Design and Fabrication of AlN SAW Resonators for Measuring Particulate Matter Characteristics

MSc thesis project

Chong Zhan

Delft University of Technology

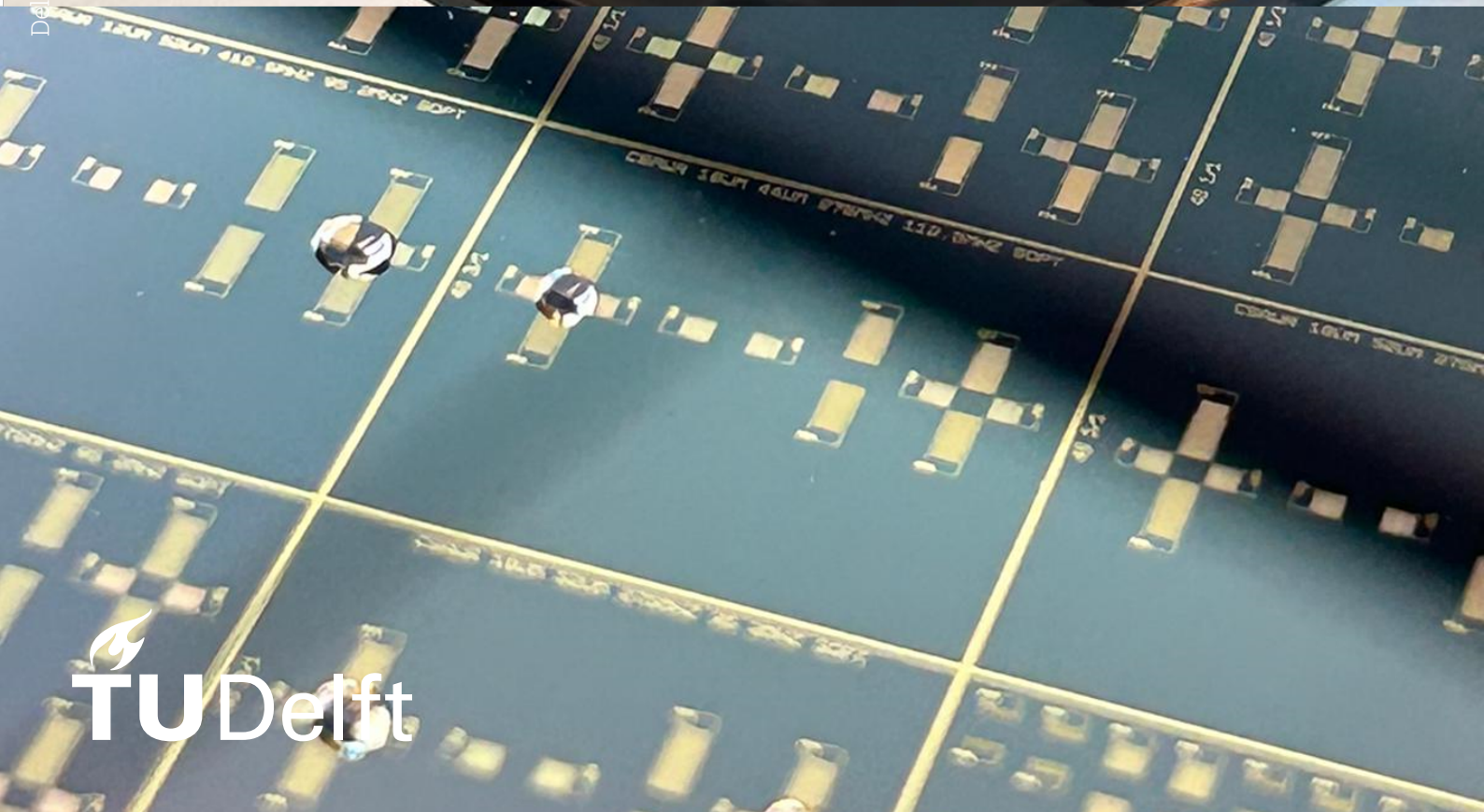

TU Delft

Design and Fabrication of AlN SAW Resonators for Measuring Particulate Matter Characteristics

by

Chong Zhan

to obtain the degree of Master of Science

at the Delft University of Technology,

to be defended publicly on Friday January 27, 2024 at 14:00 PM.

Student number: 5655781

Project duration: September 1, 2023 – September 27, 2024

Thesis committee: dr. T. Manzaneque, TU Delft, supervisor
prof.dr.ir. L. Abelmann, TU Delft

Cover: Fabricated SAW resonator with PM loading

TU Delft

Abstract

In the rapidly advancing field of industrial technology, the demand for enhanced accuracy in environmental Particulate Matter (PM) monitoring has intensified. The Background Section explores the potential of Micro-Electro-Mechanical Systems (MEMS) technology in developing high-resolution, sensitive, and portable devices for PM mass and size detection. The Second and Third Sections provide an overview of the working principles of various acoustic devices and discuss both conventional and advanced PM sensing methodologies. The Piezoelectric Material Alternatives Section concludes with a comparative analysis of different piezoelectric materials.

Design parameters were determined through simulations, as discussed in Section Five, leading to the successful fabrication of a 95 MHz-412 MHz cross-structure SAW resonator in the TUDelft Else Kooi Laboratory cleanroom, detailed in the Fabrication Section. The change in resonant frequency of the device was measured using a Vector Network Analyzer (VNA) probe station, as outlined in the Measurement Results and Discussion Section. The results demonstrate that the device can effectively detect mass loading surface perturbations generated by a 40 μm diameter, 200 nm high aluminum column in the detection region, despite its inability to sense actual 15 µm SiO2 particle clusters. Finally, the Reflection and Recommendations Section summarizes the project and offers suggestions for future development.

Contents

List of Figures

List of Tables

1

Background

Particulate Matter(PM) consists of minuscule solid particles or aerosols suspended in the air, comprising materials such as dust, dirt, soot, smoke, and microscopic substances [1]. These particles exhibit varying sizes and are commonly categorized based on their diameter. Commonly used size classification methods divide airborne particles into three main categories: coarse particles (PM10), with diameters between 2.5 and 10 micrometers, visible to the naked eye and often arising from mechanical processes or natural sources like dust storms. These particles are small enough to be inhaled into the respiratory system and can potentially reach the lungs. Fine particles (PM2.5), ranging from 0.1 to 2.5 micrometers, originate from combustion processes and remain suspended in the air for longer duration. These are even finer particles that can penetrate deeper into the respiratory system and are associated with more significant health risks. And ultrafine particles, with diameters less than 0.1 micrometers (PM0.1), produced during combustion activities, possess high reactivity and potential health concerns as they can enter the bloodstream [2].

These categories play a crucial role in assessing air quality, implementing pollution control measures, and understanding the associated health impacts.

1.1. Hazards of PM

PM pollution is a major global concern with far-reaching implications for both the environment and human health. This section aims to provide a broad exploration of the multifaceted hazards associated with PM. It will encompass various sizes and sources of PM, addressing their impacts on both the environment and human health.

1.1.1. Environmental Hazards

PM has been found to have adverse effects on vegetation. Studies indicate that heightened concentrations of PM can diminish photosynthesis, cause harm to plant tissues, and impede overall growth [3]. These consequences may have far-reaching effects on ecosystems and agricultural productivity.

The deposition of PM into water bodies poses a threat to aquatic ecosystems. Fine PM can diminish light penetration, impacting photosynthesis in underwater plants, and compromising the health of aquatic organisms [4].

PM, often carrying heavy metals and other contaminants, contributes to soil pollution. This contamination may negatively impact soil fertility, crop quality, and can have enduring consequences [5].

The emissions of PM through human activities not only contribute to environmental pollution but also induce climate changes. Coarse dust and fine non-light-absorbing inorganic aerosols, such as sulfate,

have the capacity to strongly absorb and re-emit thermal radiation under resonance conditions at long wavelengths, resulting in an increase in ambient temperature [6].

1.1.2. Human Health Hazards

Inhaling PM, especially fine particles such as PM2.5, can have detrimental consequences for our respiratory system. Such repercussions include the exacerbation of conditions like asthma and bronchitis, as well as the damaging of lung function [7]. Continuous and long-term exposure to such minuscule particles could escalate the chances of experiencing chronic obstructive pulmonary disease (COPD) and even lung cancer [8].

Scientific studies have consistently shown a robust correlation between exposure to particulate matter and an increased susceptibility to cardiovascular diseases. This includes afflictions such as heart attacks and even strokes [9]. Inhaling these harmful particles triggers a state of inflammation, overlaid by considerable oxidative stress within the cardiovascular system.

Numerous contemporary epidemiological studies consistently underscore a robust connection between exposure to particulate matter and a premature shortening of one's lifespan. It has been deduced that excessive exposure to this category of air pollutant is likely to curtail longevity significantly [10].

Adding to this is nascent research that highlights the potential of PM to impair the central nervous system detrimentally, paving the way for neurodegenerative ailments and provoking the incidence of cognitive decline [11].

The problem of particulate matter pollution poses a considerable risk to both our surrounding environment and the well-being of every single person, making it a supreme area of concern. A deep and thoughtful exploration into the heightened effects resulted from this pollutant will undeniably be a beacon of guidance in processing effective policies and enacting calculated interventions.

1.1.3. Traditional PM Sensing Methods

PM derives from a variety of sources, including transportation, industrial emissions, construction activities, and natural occurrences such as wildfires. To effectively regulate PM emissions and monitor air quality, it is crucial to accurately measure PM levels in the environment.

Measuring both the mass and size of PM is essential. The Beta Attenuation Monitoring (BAM) technique shown in Figure: 1.1(a), widely employed in air monitoring, relies on the absorption of beta radiation by solid particles extracted from airflow. This method enables the detection of PM10 and PM2.5, monitored by most air pollution regulatory agencies [12]. Additionally, the Aerodynamic Particle Sizer(APS) shown in Figure: 1.1(b) measures the real-time size distributions of particles [13].

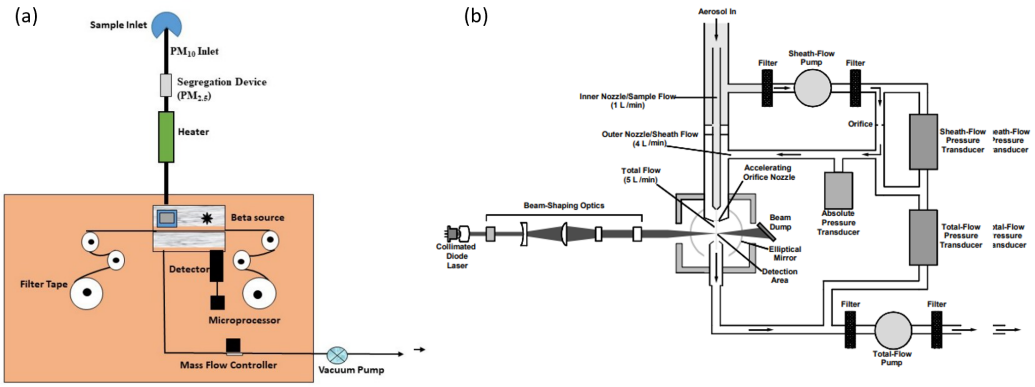

Figure 1.1: (a) Schematic of BAM (Met One BAM-1020[14]), and (b) Aerosol Flow Through the APS Model 3321[15]

While traditional methods offer well-established and accurate measurement standards, the development of Micro-Electro-Mechanical Systems (MEMS) technology introduces sensors distinguished by their miniaturization, low power consumption, and potential integration into compact, portable devices.

2

PM Mass Sensor

This section will delve into different mass measuring methods utilizing MEMS/NEMS devices, focusing on presenting the working principles and a comparison of different measurement techniques.

2.1. Mechanical Resonators as Mass Sensors

Acoustic wave-based MEMS sensors utilize the principles of acoustic wave propagation to detect and quantify changes in mass at a microscale level. The primary advantage of employing these transducers lies in their capacity for label-free recognition of the target analyte, eliminating the need for any external reagent or chemical.

2.1.1. Quartz Crystal Microbalance

The Quartz Crystal Microbalance (QCM) has emerged as a highly sensitive technology for the precise measurement of PM mass. It consists of a tiny, flat crystal with metal coatings on each side shown in Figure: 2.1(a). Originally designed for monitoring thin film deposition [16], the QCM's versatility has found new applications in environmental science, particularly in assessing air quality by quantifying PM mass concentrations [17]. This innovative approach leverages the QCM's ability to detect minuscule changes in the resonance frequency of a quartz crystal, which occur when particles deposit on its surface.

A QCM sensor based on a novel bromophenol blue doped polypyrrole nanostructure was developed to detect trace amounts of nitro-explosive vapors in ambient air with high sensitivity and selectivity [18]. Highlighting the possibilities of making QCM a valuable tool for studying air pollution, industrial emissions, and other sources of particulate matter.

2.1.2. FBAR devices

The Film Bulk Acoustic Resonator (FBAR) is a typical kind of bulk acoustic wave device, which consists of a thin piezoelectric film sandwiched between two metal electrodes, forming a resonant structure shown in Figure: 2.1(b). When subjected to an alternating electrical field, the piezoelectric material undergoes mechanical vibrations, generating an acoustic wave within the device. This wave is highly sensitive to changes in the physical properties of the FBAR, such as mass loading or temperature alterations [19].

Similar to QCM, the FBAR also operates on the principle of monitoring the resonance frequency shift caused by the accumulation of particles on its surface. However, compared with QCMs, FBARs offer better sensitivity in resonance frequency shifts when detecting tiny base mass PM [20].

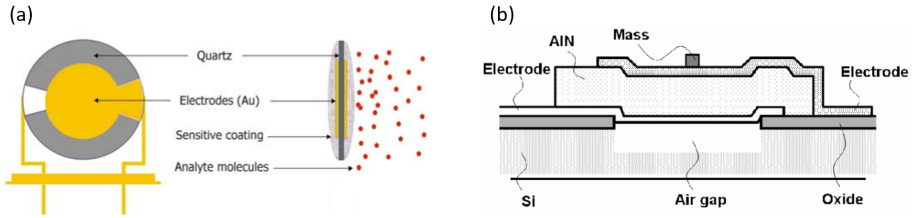

Figure 2.1: (a) Schematic of QCM sensor[21], and (b) Schematic of FBAR mass sensor[22]

2.1.3. SAW Devices

Surface Acoustic Wave (SAW) device generates and propagates Rayleigh or Love waves along the surface of a piezoelectric substrate to sense changes in the physical properties of the material on the surface[23]. These propagated waves are typically excited and detected using interdigital transducers (IDTs), which are pairs of metal electrodes connected in two groups on the surface of the material shown in Figure: 2.2. The characteristics of the detected wave signal, such as its frequency and amplitude, provide information about surface interactions of this device, such as mass loadings, conductive changes, analyte shape, and other factors.

Two typical designs of SAW sensors are illustrated in Figure: 2.2. In an acoustic delay line (ADL) SAW device, two IDTs are positioned at a specific distance from each other. The region between these IDTs is referred to as the delay line, and it is commonly used for placing PM to be measured.

When the propagating acoustic wave reaches the second set of IDTs, it is detected and converted back into an electrical signal. The time delay between the transmission and reception of the wave serves as a means to measure the time-based characteristics of the system.

In SAW resonators, reflection gratings are consciously placed at end of IDTs to reflect the acoustic wave. This results in the acoustic wave being reflected back from these gratings to the IDTs for detection. The typical structure of a two-port SAW resonator is illustrated in Figure: 2.2(b).

Similar to the SAW ADL, an electrical signal is applied to one set of IDTs on a piezoelectric substrate to generate a surface acoustic wave. Simultaneously, the electrical signal generated during detection yields insights into the resonant frequency and characteristics of the Surface Acoustic Wave (SAW) within the resonator. The observed frequency shift following mass loading is indicative of alterations in surface properties.

Thin film Surface Acoustic Wave (SAW) devices have garnered significant attention in recent literature, showcasing advancements in increased sensitivity [24], miniaturization and reliable temperature stability [25].

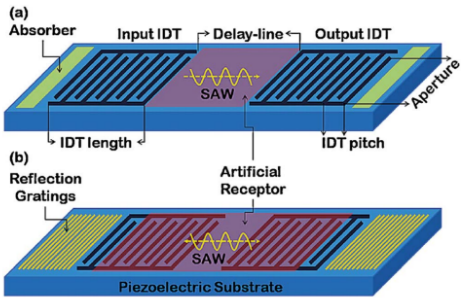

Figure 2.2: (a) delay-line and (b) resonator. Reprinted from [26]

Table:2.1 provides a comparative analysis of the performance and operating conditions observed in various research findings across different analytes using these three structures discussed above.

Table 2.1: QCM, FBAR and SAW comparison table

Analyte		Structure	Sensitivity	Limit of Detection	Operating Condition/ Comments
Ultrafine particles (nanoparticles)	organic chemical compound: Acetaldehyde (0.5 nm)	QCM [27]	4.5 Hz/ppm	27 ppm	Exposure to acetaldehyde vapor with different concentrations ranging from 100 to 500 ppm
	organic chemical compound: isopropyl alcohol (IPA)	FBAR [28]	2.54 $\mathrm{kHz/pg}$, or 0.45 $\mathrm{kHz/(ng \cdot cm^{-2})}$ normalizing to the area of the FBAR	-	A frequency deviation of 0.75 MHz was measured across two sensor oscillators.
	organic chemical compound: methanol ink particles	ZnO-based FBAR[29]	5 $\mathrm{kHz/(ng \cdot cm^{-2})}$	-	A thermal annealing was also performed to improve the deposited $\mathrm{W/SiO_2}$ multi-layer reflector.
	cat allergen powder (0.2 - 0.5 μm)	QCM with a gold-coated quartz crystal[30]	0.056 $\mathrm{Hz/(ng \cdot cm^{-2})}$	5.2 ng/L	5 MHz crystal at 20 $^{\circ}$C, conditioned room air (average RH = 41.2%) was used to convey the powder into the exposure chamber.
Fine particles	polystyrene (1-4 μm)	QCM-D [31]	-	-	Using QCM-D to measure properties. Showing how to clean the QCM sensor.
	<2.5 μm	QCM with 9.9780 MHz nominal frequency AT-cut [32]	1.6 Hz/mg	0.147 $\mathrm{mg/m^3}$	Conducted in a controlled exposure chamber with a room temperature of 25$\pm$0.3°C and 65$\pm 0.3\% of humidity$
	commercial silicon dioxide particles (0.1 - 4 μm)	An aluminum nitride (AlN) based SAW sensor[33]	33.82 kHz/ug	with adhesive film: 20.45 $\mu\mathrm{m/m^3}$ without: 9.95 $\mu\mathrm{m/m^3}$	The suspended silicon dioxide particles with a diameter in the range of 0.1–4 μm were bubbled into the virtual impactor for 5 mins and the PM in one of the major flow were collected by putting a silicon wafer at its outlet.
Coarse particles	PM10: incense smoke	QCM consists of a cascade impactor[34]	-	-	The proposed system consists of an OPC and QCM is capable of measuring PM10 in the air at various times and spaces.
	Arizona dust	Aluminium nitride based FBAR[35]	27.5 $\mathrm{Hz/(\mu gm^{-3})}$	50 $\mu\mathrm{g/m^3}$	A TOPAS SAG410L aerosol generator is set up with a compressed zero air supply to feed aerosolized type Arizona dust into a sealed 370 L glass tank at 1 bar air pressure.
Mixture	gold particles (0.75 μm and 20 μm); fine sugar (8 μm); PTFE (1μm and 15 μm)	SAW Resonator[36]	average mass sensitivity of 275 Hz/ng	-	The particle sensors were designed to resonate at a frequency of 262 MHz. They were made up of aluminium based inter-digital-transducers (IDTs) patterned on top of ST-cut quartz substrate.
	PM2.5 and PM10	SAW delay line[37]	0.03 $\frac{m^{\circ}/s}{\mu g \cdot m^{-3}}$	1 $\mu g/m^3$	Particle separation based on aerodynamic diameter is achieved using a 3 Lpm dedicated cascade impactor.

2.2. Nano-mechanical Spectrometry

Mass spectrometry shown in Figure: 2.3(a) is also a robust analytical technique, which utilises the mass-to-charge ratio to separate and detect the resulting ions from the ionization of sample molecules in the gas phase. Widely applied for measuring molecular species within the range of 100 Da to 100 kDa with exceptional precision [38], its efficacy encounters challenges when confronted with heavier species, such as nanostructures and biological assemblies, leading to a notable decline in performance [39].

In 2016, researchers at the Institute of Microelectronics of Madrid (IMM-CSIC) developed a theoretical method capable of determining the mass, position, and stiffness of analytes on a cantilever device. This innovative approach relies on analyzing resonance frequency jumps observed in the microcantilever resonator vibrating at different frequencies shown in Figure: 2.3(b). Those resonance frequency jumps can be used to derive mass, position and stiffness information for analytes in contact with the cantilever surface.[39].

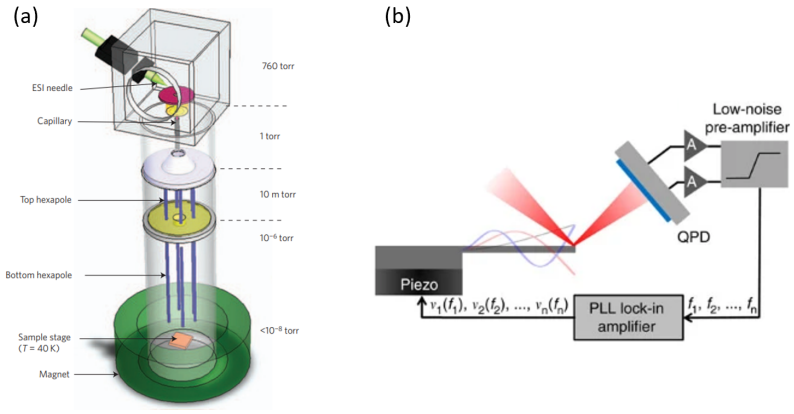

Figure 2.3: (a) Simplified schematic of MS[40] and (b) Schematic of microcantilever vibration modes detection. Reprinted from [39]

2.3. Comparison of Different Mass Sensor

While QCM, FBAR, and SAW mass sensors operate on similar principles, distinctions in MEMS construction and the materials employed contribute to variations in their performance, making them suitable for different scenarios. The performance characteristics of QCM, FBAR, and SAW mass sensors, including aspects such as operating frequency, dynamic range, sensitivity, material, and more will be discussed in this part.

Most commonly used and commercially accessible QCMs typically utilize frequencies within the range from 5 to 20 MHz [41]. Since QCM is the Quartz thickness shear mode (TSM) resonator [42], whose resonating frequency depends on the thickness of the piezoelectric substrate. Theoretically, it is possible to reduce the thickness to get a High Fundamental Frequency(HFF) QCM, but reducing the thickness will lead to structural instability. The working frequency of FBAR devices can reach 10 - 20 GHz easily with piezoelectrical layer thickness of μm level [43]. The operating frequency of a Surface Acoustic Wave (SAW) device depends on the wavelength of the electrodes and neighboring spaces, a wavelength of 40 µm easily generates an operating frequency of nearly 78 MHz [44].

Based on Sauerbrey's relation [45]:

$$\Delta f = -\frac{2f_0^2}{A\sqrt{\rho_q \mu_q}}\Delta m \tag{2.1}$$

Where f_0 is the resonant frequency of the fundamental mode, Δf is the normalized frequency change, Δm is the mass change, A is the piezoelectrically active area, ρ_q is the density of piezo material and μ_q is the shear modulus of piezo material. Based on the equation mass sensitivity is directly proportional to the square of resonance frequency. As a result, the approximate sensitivity ranking can be established as follows: FBAR, SAW, and QCM. It is important to note that mass sensitivity is influenced by various factors, including the choice of piezoelectric material, the piezoelectrically active area, and others. The provided ranking only represents a general trend.

The Limit of Detection (LoD) is a fundamental parameter in PM mass detection that defines the lowest mass concentration of an analyte that can be reliably detected. It represents the threshold below which the signal from the sensor is indistinguishable from the background noise. In other words, the limit of detection indicates the point at which the signal-to-noise ratio becomes too low for accurate and confident measurement. And LoD of PM mass sensor is determined by using geometry, piezoelectric material and detecting area. The mass concentration LoD (in weight per cubic meter) of the mentioned PM mass sensors are mainly around $\mu g/m^3$ [46] [47] [48] and when both use Virtual Impactor(VI) as a PM size separator, SAW has better LoD.

All these acoustic devices work efficiently in a gaseous environment since properties like air density, viscosity, conductivity, and surface charge minimally impact the oscillations of acoustic resonators. It's worth noting that for liquid environment measurements, there is always a damping of acoustic energy. Due to the nature of QCMs as TSM resonators that generate shear acoustic waves without significantly radiating energy into the liquid medium, they stand as the most extensively researched acoustic sensors for measurements in liquid environments [49] [50].[50]. The table below gives an overview of QCM, FBAR, and SAW.

Table 2.2: QCM, FBAR and SAW comparison table

	QCM	FBAR	SAW
Acoustic Wave Type	Bulk (shear mode)	Bulk (longitudinal mode)	Surface (rayleigh mode)
Working Frequency	5-20 MHz	10-20 GHz	Hundreds of MHz
Sensitivity (Mass)	$\sim$ 1 $\mathrm{Hz}/(\mathrm{ng}\cdot\mathrm{cm}^{-2})$ (low sensitivity)	$\sim$ 2.4 $\mathrm{kHz}/(\mathrm{ng}\cdot\mathrm{cm}^{-2})$ (high sensitivity)	Excellent sensitivity in comparision to QCM.
Limit of Detection	15 $\mu g/m^3$	18 $\mu g/m^3$	1 ppb ($\approx 2.445 \mu g/m^3$)
Size and Integration	Compact and can be integrated into various analytical instruments.	Typically smaller than QCM, enabling miniaturization in electronic devices.	Highly compact and suitable for integration into portable and wearable devices.
Piezoelectric Materials	Quartz	AlN, ZnO, PZT	Quartz, LiNbO3 , LiTaO3, AlN
Working Medium	Liquids and Gases	Liquids and Gases	Gases

3

Methods of Distinguishing PM Size

As mentioned earlier in this review, PM is categorized based on its dimensions. Therefore, comprehending and characterizing the size distribution of PM becomes essential for evaluating air quality and potential health impacts. This chapter explores various methods devised to differentiate PM sizes, categorizing them into two forms: optical devices, additional separators, and mechanical resonance-based techniques.

3.1. Particle Size Analysis with Optical Counter

The Optical Particle Counters (OPC) operate on principles of light scattering or blockage to estimate particle size distribution. The Figure: 3.1(a) shows that the presence of opaque particles in the sampling volume produces a light-obscuring shadow effect. Often used for real-time monitoring owing to its ability to provide particle-size distribution across a broad spectrum. However, they are less suitable for atmospheric pollution analysis, containing particles of diverse compositions, as they can only provide the optical diameter rather than the aerodynamic diameter from light scattering [51]. Moreover, it's difficult to obtain mass concentration from the optical analysis method.

3.2. Particle Size Analysis with Additional Separators

Separating PMs of a particular size for individual measurement is an important method in particle size analysis. However, this method often requires additional equipment for PM separation. Some of the different PM separation techniques are discussed below.

The Scanning Mobility Particle Sizer (SMPS) shown in Figure: 3.1(b) operates by generating charged particles from a polydisperse aerosol, introducing them into an electric field for size-based separation using a differential mobility analyzer (DMA), and then detecting and analyzing the size-segregated aerosol to generate a high-resolution particle size distribution [52]. SMPS measures the electrical mobility of charged particles in an electric field, offering high-resolution size distribution data, particularly for ultrafine and fine particles [53].

The Electrical Low-Pressure Impactor (ELPI) shown in Figure: 3.1(c) functions by charging aerosol particles, subjecting them to an electric field for aerodynamic classification, and directing them with impactors onto a series of collection surfaces based on their size [54]. An impactor is a device that separates particles based on inertia, typically extracting particles within a specific size range from the sample flow [55]. It either collects them for subsequent analysis or eliminates them to prevent issues related to instrument contamination. Additionally, impactors are commonly cascaded to collect particles of varying size ranges on distinct substrates for chemical or gravimetric analysis [51]. Since impactors rely on inertia and aerodynamic forces to separate PMs of different sizes, the structure of the impactor

can have a significant impact on the separation results, leading to large measurement errors.

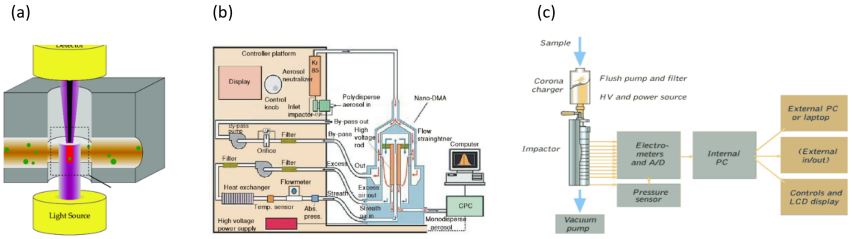

Figure 3.1: (a) Schematic of OPC [56], (b) Schematic of SMPS [57], and (c) Schematic of ELPI. Reprinted from [58]

3.3. Particle Size Analysis with Structure-based Techniques

Unlike optical devices and additional separators, some special structures are used in order to measure the PM mass concentration in real-time while resolving the PM size without using bulky separators.

3.3.1. Multimode Frequency Shift Method

Within the resonant sensor, the adsorption of an individual analyte on its detecting area induces different effects on each vibration mode. Those adding analytes always caused a frequency shift at different vibration modes. And these multimode frequency shifts are experimentally proved to be related to the inertial mass, position of adsorption, and the size and shape of individual analytes [59]. In reference [60], a reversing algorithm has been derived from the famous one-dimensional resonator beam frequency shift:

$$\frac{\delta f_n}{f_n} \approx -\frac{m_{added}}{2M_{device}}\Phi_n^2(x) \tag{3.1}$$

to derive from cantilever frequency shifts under multimode to position, aerodynamic radius, and mass of a single analyte. Where δf_n is the change in resonant frequency of the device upon mass adsorption, f_n is the resonant frequency of the device without the adsorbate, m_{added} is the adsorbed mass at position (x), M_{device} is the device mass, and $\Phi_n(x)$ is the normalized displacement mode shape of mode n. And it has been proved that at least 5 multimodes should recorded to get an accurate reversing result. Meanwhile, the spatial extent of observing analyte can not exceed 30% of the resonator device, otherwise the predictions are poor.

3.3.2. Mass & Elastic Region Method

The SAW frequency shift perturbed by starch granules with a radius of 0.625μm under different excitation frequencies is simulated by Yang [61], which is shown below:

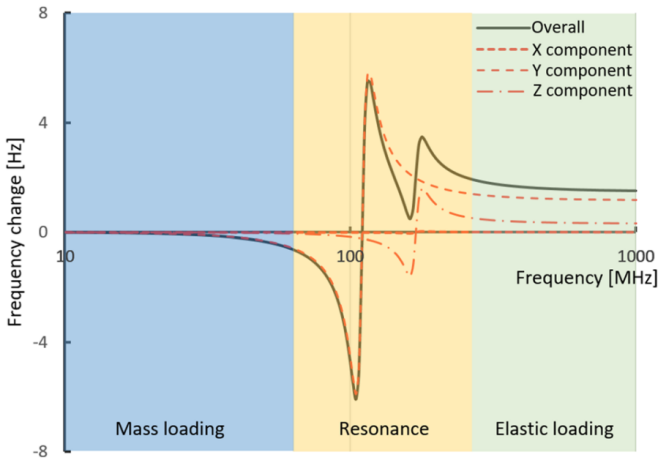

Figure 3.2: The relationship between the frequency change and SAW operation frequency for starch granules with a radius of 0.625μm. Reprinted from [61]

The particle-induced perturbation to the sensor can be classified into three regimes based on the direction of the frequency changes: the low-frequency mass loading regime, the high-frequency elastic loading regime, and the transitional resonance regime in between (black solid line in Figure: 3.2). This phenomenon arises because the particle-SAW system has different degrees of coupling at different excitation frequencies.

In the low-frequency mass loading regime, characterized by coupled vibrations, the particle essentially adheres rigidly to the sensor surface. The particle's movement is in-phase with the interface, resulting in harmonic motion around the equilibrium position of the interface. Simply put, the particle vibrates in unison with the surface.

Conversely, in the high-frequency elastic loading regime, where the coupling is weak, the particle is loosely connected to the sensor surface through a soft stiffness. Stress is concentrated near the contact interface, causing the primary body of the particle to remain stationary, as if clamped. In essence, the sensor surface compresses the particle.

It has been experimentally verified[62] that when SAW devices operate beyond 260MHz, starch particles exhibit behavior consistent with the Elastic Loading regime. The observed frequency change in these starch particles, with radius r ranging from 2μm to 50μm, conforms to a proportional relationship with $r^{2/3}$, demonstrating a ratio of 18$\mathrm{kHz}/\mathrm{m}^{2/3}$. In some measure, this ratio can be used to distinguish PM with different properties. As a result, utilizing SAW resonators at different frequencies allows for the extraction of size distribution using a suitable algorithm.

Both the multimode frequency shift and the Mass & Elastic region methods only rely on the structural properties of the resonator for real-time analyte dimension measurements. However, specific requirements and limitations persist. For instance, the multimode frequency shift method necessitates recording frequency shifts under at least 5 mode shapes. The Mass & Elastic region methods require SAW devices capable of adjusting their operating frequency between low (Mass region around 1MHz-10MHz) and high (Elastic region around 100MHz-1000MHz) frequencies, with certain properties of the tested PM needing prior knowledge. Additionally, both methods mandate a suitable reversing algorithm for extracting size and mass results.

4

Piezoelectric Material Alternatives

Acoustic devices can be made using a variety of natural or synthetic piezoelectric substrates, with the piezoelectric properties of each material contingent on its cutting angle. To develop a high-frequency acoustic device, it is essential to compare materials and their specific cutting angles. Quartz has consistently been the preferred primary piezoelectric material due to its high quality factor, straightforward design, wide availability, and cost-effective fabrication. And the AT-cut quartz substrate which rotates the Y plane making its normal axis parallel to the y-axis with $\phi = 35.25°$ (shown in Figure: 4.1) is usually used to design QCMs. [63].

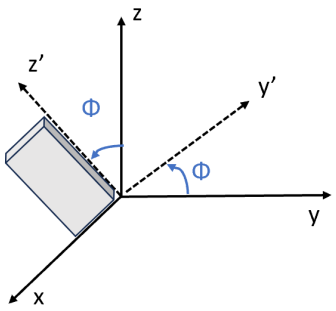

Figure 4.1: AT-cut quartz crystal wafer. ϕ is the cut angle.

AlN stands out as a widely utilized piezoelectric material due to its compatibility with high-temperature fabrication processes. Its remarkable acoustic velocities (10.8 km/s in Longitudinal mode, 6.1 km/s in Shear mode) surpass those of many other piezoelectric materials, facilitating higher operational frequencies [64]. This characteristic enhances the feasibility of implementing the Mass & Elastic region size discrimination method. Despite these advantages, the electro-mechanical coupling factor of AlN is constrained ($\mathrm{K}^2 = 9.7\%$ in Longitudinal mode, $\mathrm{K}^2 = 2.3\%$ in shear mode). To address this limitation, doping AlN-based resonators with scandium has been explored as a compensatory measure [65]. However, in a gaseous medium for PM detection, the resonator encounters significantly less damping compared to its operation under a liquid medium. This means that AlN can already provide sufficient electro-mechanical coupling factor

In contrast, alternative piezoelectric materials often encounter challenges such as CMOS incompatibility or low acoustic velocity. For instance, while PZT demonstrates a commendable electro-mechanical coupling factor ($\mathrm{K}^2 = 56\%$ in Longitudinal mode, $\mathrm{K}^2 = 45\%$ in shear mode), its usage is hindered by its toxicity due to the presence of lead. This underscores the need for careful consideration of material properties and fabrication compatibility when selecting piezoelectric materials for specific applications. The table provided below offers a comparative overview of quartz, AlN and PZT.

Table 4.1: Quartz, AlN and PZT comparison table [66][67]

	AT-cut Quartz	AlN	PZT
Acoustic Velocity of transverse waves (m/s)	∼3750	∼5760	∼3900
Acoustic Velocity of longitudinal waves (m/s)	∼5965	∼11000	∼4500
Effective Electro-mechanical Coupling Factor (%)	∼8.8	∼5	∼30
CMOS Compatibility	Yes	Yes	No

5

Simulations

This section presents multiple Finite Element Method (FEM) simulations and their results, aimed at optimizing the design of a SAW resonator to detect particle mass and size characteristics on resonant frequency. Key parameters, such as electrode material, AlN layer thickness, resonator cavity length, and the structure of the reflector and IDT, are evaluated to identify an effective design. Additionally, a 3D simulation will demonstrate the impact of a single SiO2 cubic load placed at the center of a straight SAW resonator.

5.1. Simulation environment introduction

FEM simulation is a computational technique used to solve complex physical problems that are difficult to solve analytically. FEM breaks down a large, complex system like a SAW resonator, into smaller, simpler parts. Each of these elements is interconnected, forming a mesh[68]. By applying the piezoelectric equations[69] as follows to each element, FEM simulates how the system behaves under various conditions:

$$T_{ij} = c^E_{ijkl} S_{kl} - e_{kij} E_k \tag{5.1}$$

$$D_i = e_{ikl} S_{kl} + \epsilon^S_{ij} E_k \tag{5.2}$$

where T_{ij} is the stress vector, c_{ijkl} is the elasticity matrix (N/m^2), e_{ikl} is the piezoelectric matrix (C/m^2), ϵ_{ij} is the permittivity matrix (F/m), E_k is the electric field vector (V/m), S_{kl} is the strain vector, and D_i is the electrical displacement (C/m^2).

COMSOL Multiphysics is a powerful commercial software used for FEM simulations, with built-in piezoelectric equations available in its Piezoelectric Effect Multiphysics library. In this study, COMSOL Multiphysics 6.1 was used to conduct the SAW resonator simulations.

5.2. Design the SAW resonator working frequency

According to the Mass & Elastic Region method discussed in Section 3.3.2, elastic loading characteristics can be detected at high SAW operating frequencies. However, determining the exact required frequency remains a challenge. After evaluating commercially available particulate matter (PM), silica particles were selected for the experiment due to their accessibility, ease of handling, and safety (non-toxic, non-radioactive). To identify an appropriate high frequency, a SiO2 sphere eigenfrequency simulation was conducted to estimate the operating frequency range.

As shown in Figure 5.1(a), a SiO2 sphere, fixed at a small area on the bottom and with a diameter ranging from 4 to 40 μm, was modeled to determine its breathing mode resonant frequency. And the

simulated eigenfrequencies are listed in Table 5.1.

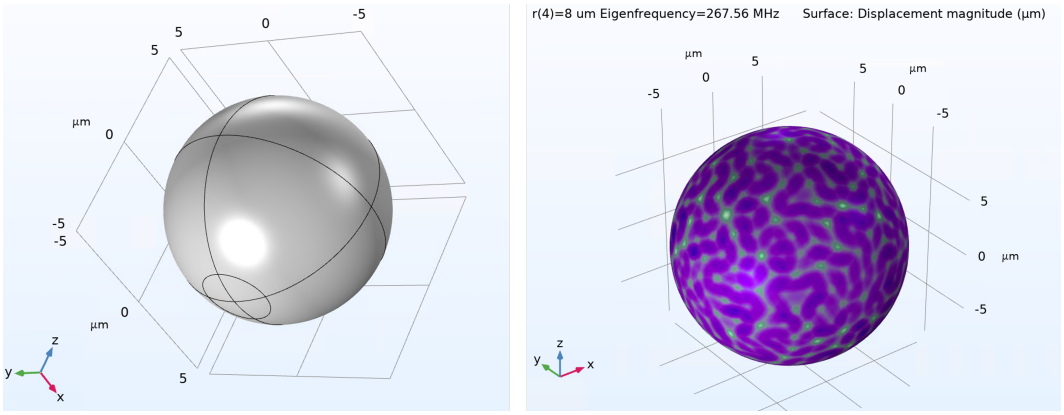

Figure 5.1: (a) Schematic diagram of the SiO2 sphere eigenfrequency simulation, (b) 16 μm diameter breathing mode resonant frequency

Table 5.1: Breathing mode eigenfrequency of SiO2 spheres with diameters ranging from 4 to 40 μm

SiO2 sphere diameter (μm)	Eigenfrequency (MHz)
4	1070.2
8	535.12
12	356.75
16	267.56
20	214.05
24	178.37
28	152.89
32	133.78
36	118.92
40	107.02

Based on the simulation results in the Table 5.1, it is evident that the eigenfrequency of SiO2 particles decreases significantly as the particle diameter increases. For the purposes of simulation in this chapter, the SAW device will be modeled near the frequency of 267.56 MHz, which corresponds to a particle diameter of 16 μm. The detailed selection of the high and low frequencies used in the Mass & Elastic Region method will be further explained in Section 6, Layout Design.

5.3. Design the thickness of AlN layer

In addition to its relatively high piezoelectric properties, AlN is the preferred material for various applications requiring excellent electrical isolation[70], CMOS compatibility, and a high surface acoustic wave velocity, all of which are crucial for the development of surface acoustic wave devices.

It has been shown that the thickness of piezoelectric films has a notable impact on the propagation loss of SAW devices[71]. For AlN thin films, piezoelectric coefficients d_{33} and d_{31} increase with AlN film thickness (ranging from 300 nm - 2400 nm)[72]. A 3D COMSOL model of a 260 MHz 2-port SAW resonator with 20 pairs of IDTs and 20 reflectors (Figure 5.2) was built, simulating AlN film thicknesses of 800, 900, and 1000 μm.

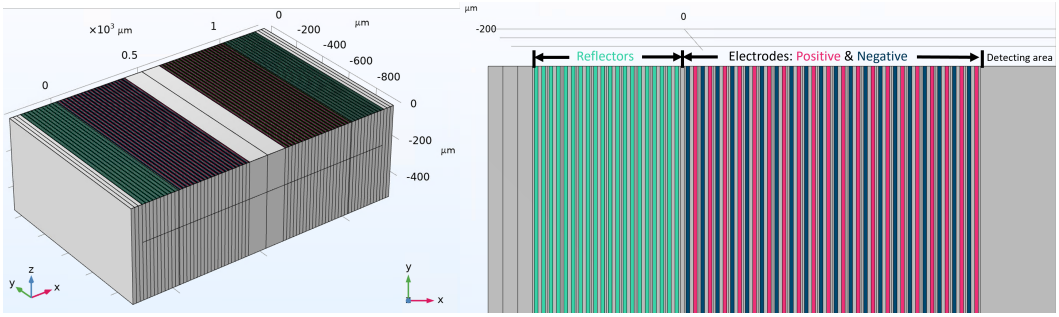

Figure 5.2: Schematic diagram of the AlN thickness simulation

Based on the simulation results (Figure 5.3), the transmission S-parameter S_{12} increases with greater AlN layer thickness. However, depositing 1μm of AlN using the Trikon Sigma 204 system in the EKL cleanroom would take more than half an hour. Since a -50 dB transmission parameter is sufficiently high to distinguish from noise level in later measurements, 1μm thickness is considered adequate.

AlN thickness (nm)	S12 at 258MHz (dB)
800	-63.864
900	-55.422
1000	-53.497

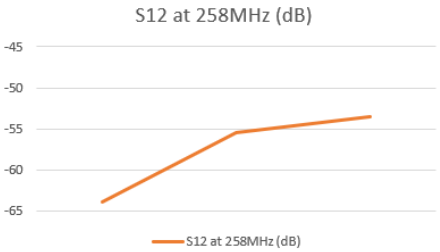

Figure 5.3: S12 with AlN film thickness at 800, 900 and 1000μm

5.4. Choose electrode material between Al and Au

In terms of IDT electrode design, the author choose the 50% metallization (a quarter wavelength) ratio single phase IDTs which has alternating polarity electrodes shown in Figure: 5.4 below. In order to fabricate a clear IDT pattern after e-beam evaporation and lift-off in EKL cleanroom, thickness of electrodes are settled as 200 nm.

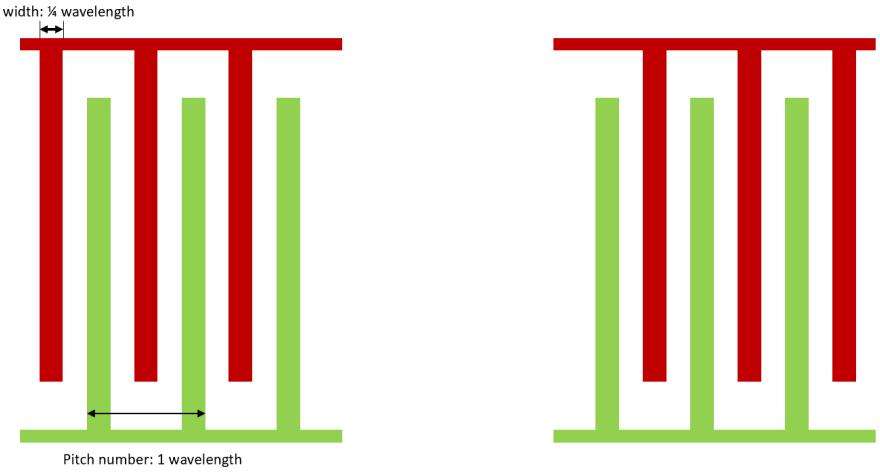

Figure 5.4: Schematic diagram of a 50% metallization single-phase IDT

Two materials were available for metal evaporation: gold and aluminum. To determine the acoustic properties of these metals as electrodes at specific SAW frequencies, eigenfrequency simulations were performed using a 1 μm AlN piezoelectric layer with wavelengths of 12 μm and 52 μm, incorporating both gold and aluminum electrodes.

The simulated eigenfrequency results are shown in Figure: 5.5.

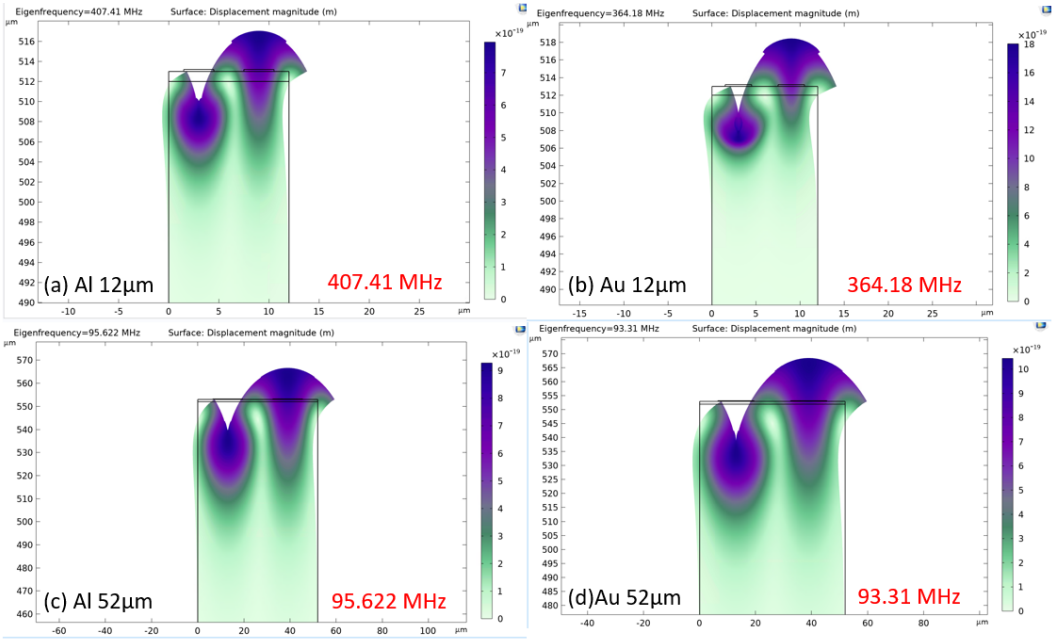

Figure 5.5: Eigenfrequency simulation with (a)Al electrodes with 12 μm wavelength; (b)Au electrodes with 12 μm wavelength; (c)Al electrodes with 52 μm wavelength; (d)Au electrodes with 52 μm wavelength

It is obvious that phase velocity of Rayleigh wave in AlN layer is effected by materials of electrodes, especially under high resonant frequency. The phase velocity can be calculated using $V_p = \lambda f$, λ and f are wavelength and resonant frequency respectively. The simulated Al and Au acoustic properties on 1 μm AlN piezo-layer with wavelengths of 12 μm and 52 μm can be concluded as:

Table 5.2: Al and Au acoustic properties on 1 μm AlN piezo-layer with wavelengths of 12 μm and 52 μm

	Aluminium	Gold
Chemical symbol	Al	Au
Density	2712 kg/m^3	19300 kg/m^3
Phase velocity, 12 μm wavelength	4888.92 m/s	4370.16 m/s
Phase velocity, 52 μm wavelength	4972.344 m/s	4852.12 m/s

Theoretically, a higher-density reflector in a SAW resonator would provide improved reflection. However, due to the resolution limits of the laser writer in the Kavli cleanroom, the IDT wavelength cannot be designed smaller than 12 μm. To detect high-frequency elastic characteristics using the Mass & Elastic Region method, the resonant frequency should be maximized. In this context, aluminum is a better choice than gold, as it achieves a higher resonant frequency for the same electrode width.

5.5. Design the length of resonator cavity

Intuitively, as the wave propagates over a longer distance in a SAW resonator, energy loss increases, reducing transmission efficiency. Additionally, the longer propagation distance causes the waves reflected by the reflectors on both sides to interfere with the forward-propagating waves, potentially shifting the resonant frequency of the resonator. Therefore, the resonator cavity length should be minimized. However, the final design must leave enough square space, equivalent to the aperture length, for the PM to make contact, making it necessary to determine the optimal resonator cavity length. Meanwhile, the aperture number of the SAW IDT is another important factor, as a larger aperture can reduce insertion loss and enhance the Q factor. Typically, the aperture size is set between 50 and 100 times the wavelength[73]. In the absence of relevant literature, a custom 407 MHz SAW resonator simulation with 15 pairs of IDTs and 10 two-sided reflectors was built to address this.

To reduce simulation time, a single longitudinal slice of the SAW resonator (as shown in Figure 5.6) was used to evaluate different resonator cavity lengths: 905.7 μm, 1811.4 μm, 3622.8 μm.

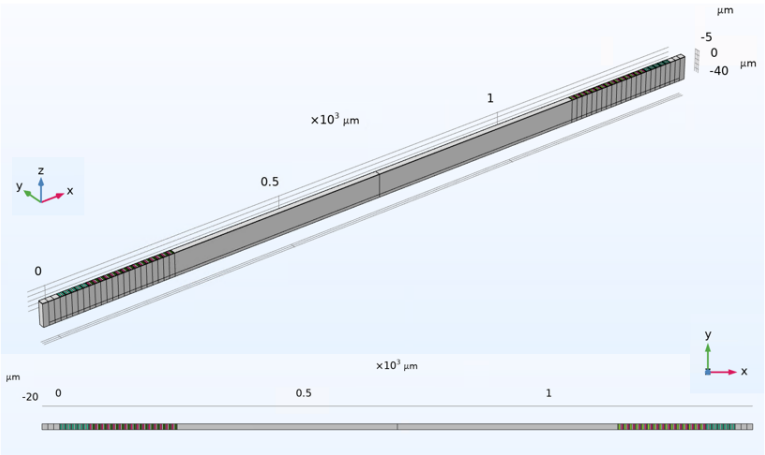

Figure 5.6: Schematic diagram of the AlN SAW cavity length simulation

The simulation results in Figure5.7 align with expectations. At a resonator cavity length of 905.7 μm, the simulated resonant frequency closely matches the theoretical frequency for a 12 μm wavelength. However, for resonator cavity lengths of 1811.4 μm and 3622.8 μm, the main resonant frequencies decrease by approximately 4 MHz and 5 MHz, respectively. Notably, as the resonator cavity length increases, the occurrence of multi-resonance becomes more pronounced. This effect is likely due to the interference between the waves reflected from the reflectors on both sides and the forward-propagating waves. Contrary to expectations, the transmission parameters S_{12} of the SAW device do not decrease significantly as the resonator cavity length increases. This is because the energy loss during wave propagation in the AlN layer was not considered in order to reduce simulation time.

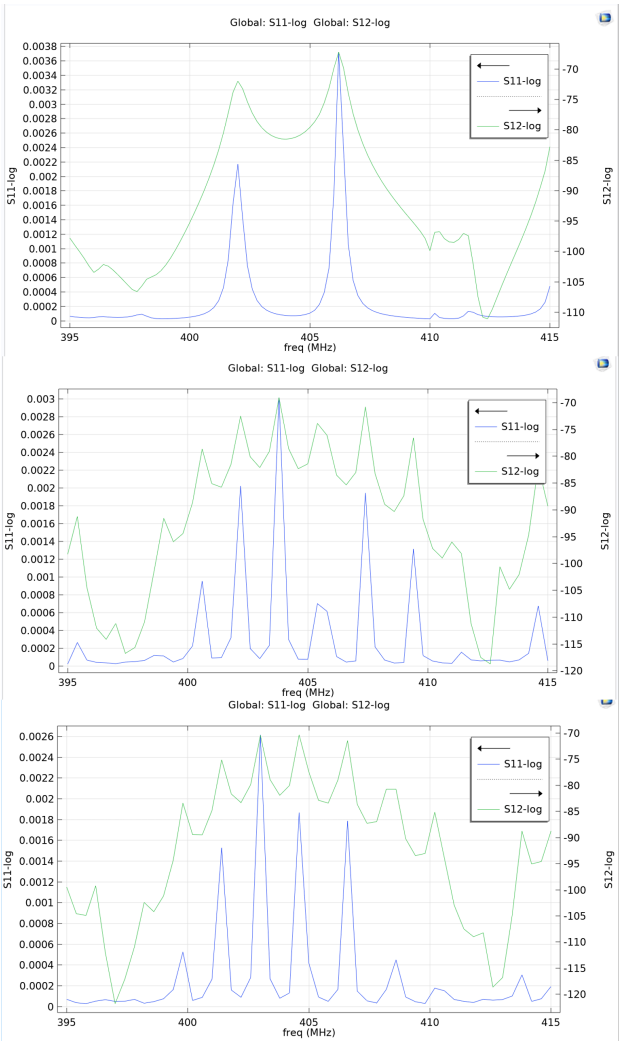

Figure 5.7: Frequency domain simulation with (a)905.7 μm resonator cavity length, (b)1811.4 μm resonator cavity length, (c)3622.8 μm resonator cavity length

5.6. Design the Reflectors & IDTs Structure

In a SAW resonator reflectors and IDTs play essential roles in generating and guiding the acoustic waves. The pair ratio between Reflectors and IDTs, and the change of total number of Reflectors and IDTs are two key parameters simulated in this section using the same 260 MHz SAW resonator as in Section 5.2 (Figure 5.2), with modifications to the IDT and reflector structures.

As shown in Figure 5.8 and Figure 5.9, it is evident that, with a constant SAW surface load weight (i.e., without altering the total number of reflectors and IDTs), increasing the proportion of reflectors brings

the main resonance frequency closer to the ideal 260 MHz. This is also consistent with the function of reflectors which help to reinforce the resonance of the acoustic waves in the SAW device[74].

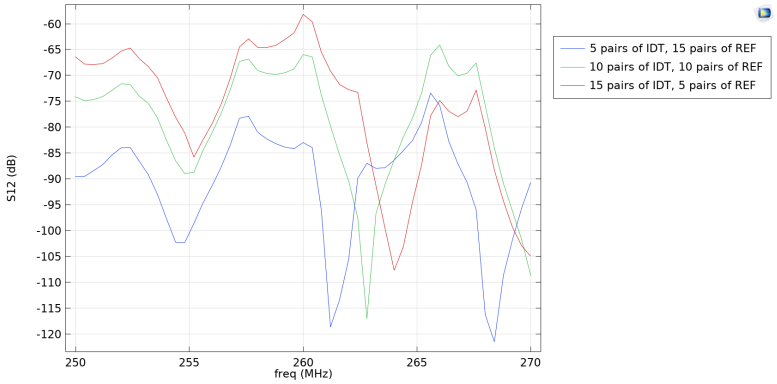

Figure 5.8: S12-parameter results with 20 total pairs and different REF/IDT pairs ratio

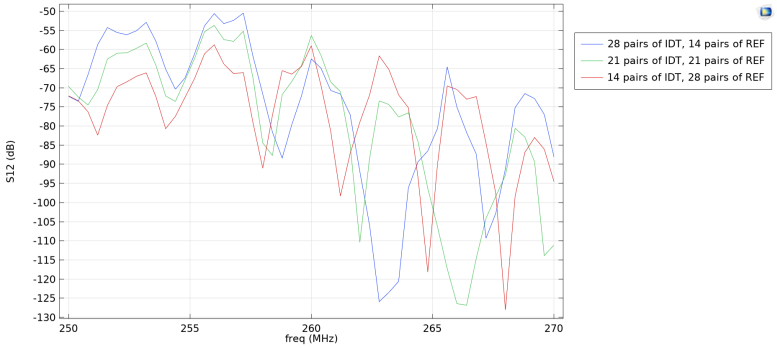

Figure 5.9: S12-parameter results with 42 total pairs and different REF/IDT pairs ratio

Comparing Figure 5.8 and Figure 5.9 shows that the occurrence of multi-resonance becomes more pronounced as the total number of devices on the SAW surface increases, when the ratio of reflectors to IDTs remains constant.

Those simulation results gave the author clues about which kinds of Reflector and IDT structures should be considered during fabrication. And a detailed fabrication structure list has been attached to Appendix A.

5.7. Scattering optimization

In a study on the scattering analysis of two-port SAW resonators, Waldemar Soluch numerically analyzed two designs with different electrode patterns using linear equations derived from the scattering matrix of the two-port resonator [75]. The results revealed that the output of the two-port resonator consists of two signals. When the IDTs are positioned at a specific point of minimum insertion loss (as described in Equations 5.3 and 5.4), these signals are in phase at the resonance frequency, and such SAW resonators are termed asynchronous resonators. In contrast, when the IDTs are placed inside the reflectors, the signals are in phase quadrature, leading to higher insertion loss; these are referred to as synchronous resonators. In simpler terms, asynchronous resonators exhibit lower insertion loss.

According to the calculations in [75], for an asynchronous resonator, the cavity distance (d1, shown in Figure 5.10) between the reflectors and IDTs, as well as the interval between the two IDT ports (d2,

shown in Figure 5.10), must satisfy the following equations:

$$d1 = (m - 0.25)\lambda \tag{5.3}$$

$$d2 = n\lambda/2 \tag{5.4}$$

where m and n are integers, and λ is the SAW wavelength.

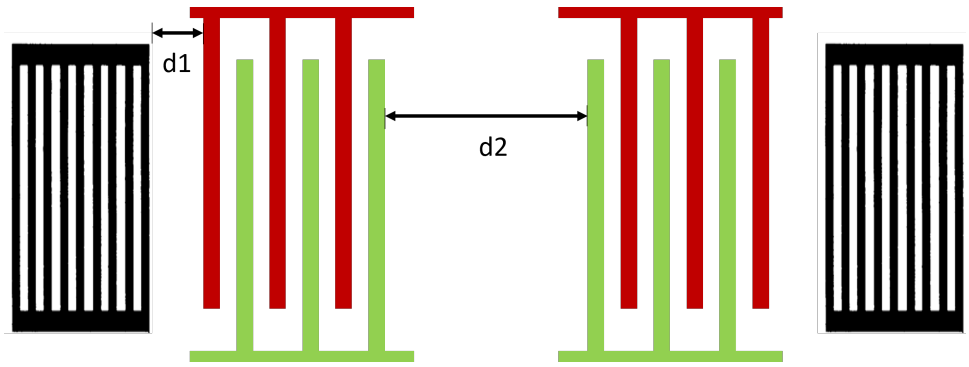

Figure 5.10: two-port SAW resonator

To evaluate the effect of scattering optimization on transmission efficiency and insertion loss in a specific SAW device, the author optimized the 259 MHz SAW resonator with 20 pairs of IDTs and 20 pairs of reflectors, following the simulations based on equations (5) (m=1) and (6) (n=100). For comparison, an alternative electrode pattern where $d_1 = 0.25\lambda$ was simulated to represent the case without scattering optimization. As shown in Figure 5.11, the results indicate that applying scattering optimization improved the transmission Y-parameter by approximately 2 dB. Consequently, the author included the scattering-optimized design in the fabrication plan, as detailed in Appendix A.

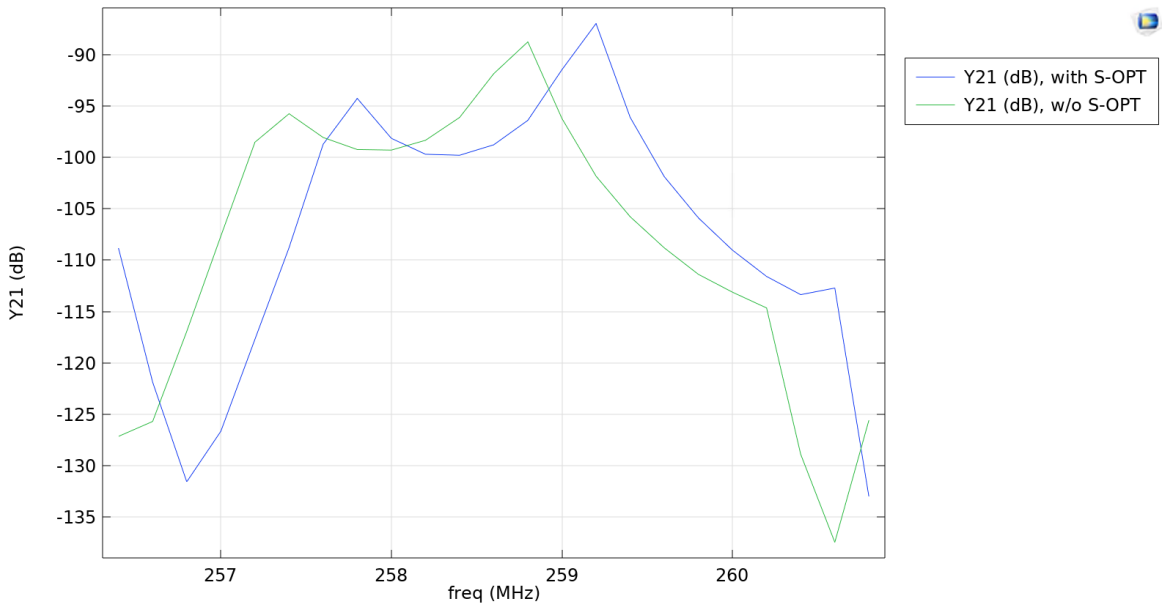

Figure 5.11: 20 pairs of REF and 20 pairs of IDT 259MHz SAW resonator, Scarttering Optimization Comparison

5.8. 3D simulation with a single SiO2 cubic on SAW cavity

Before fabricating the device, the author simulated the resonant frequency shift of a SAW resonator caused by a single SiO2 particle, as shown in Figure 5.12(a). The aim of this simulation was to evaluate the SAW resonator's ability to detect elastic loading at a relatively high resonant frequency. The frequency of 580 MHz was chosen to activate the elastic loading detection, based on the simulation results discussed in Section 5.2. Since 580 MHz is higher than the typical resonant frequency of SiO2 particles in breathing mode, it increases the likelihood of detecting the PM-SAW system within the elastic loading regime.

To simplify the meshing setup for the PM-SAW system, a small cube was used in the SAW probe region instead of the sphere PM, and a relatively small configuration of 4 pairs of IDTs and 4 pairs of reflectors was employed to reduce simulation time. Multiple triangular meshes (shown in Figure 5.12(b)) were applied to the SiO2 cube and the SAW cavity to ensure sufficient element density for accurately simulating the contact between these components. The resonant mode shape with a 1 μm cubic PM is depicted in Figure 5.12(c), clearly demonstrating that the presence of the PM alters the mode shape at resonant frequencies. From the frequency response when SiO2 is not activated (Figure 5.12(d)), it can be further concluded that the resonance frequency of the SAW resonator is specifically around 584 MHz.

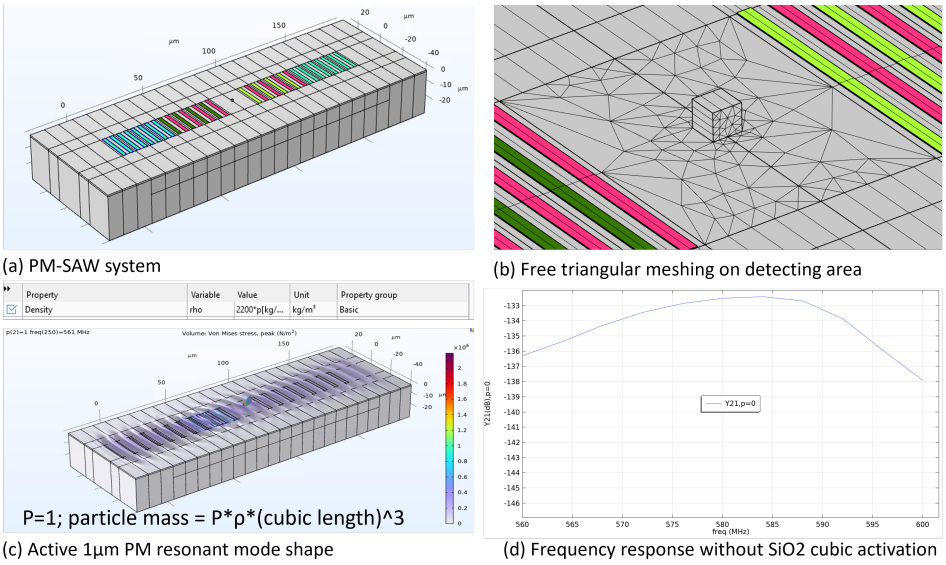

Figure 5.12: (a) PM-SAW system, (b) Free triangular meshes for SiO2 cube and SAW cavity, (c) Active 1 μm PM resonant mode shape, (d) Frequency response without SiO2 cubic activation

Cubic sizes ranging from 0.5 μm to 2.5 μm were simulated, as shown in Figure 5.13. Based on the results from Section 5.2, the resonant frequencies of these smaller SiO2 cubic particles are significantly higher than 580 MHz. According to the Mass & Elastic loading method, the detection of these SiO2 cubes falls within the elastic loading or resonance regime. The simulation results show that all resonant frequencies cluster around 583 MHz, slightly lower than the 584 MHz standard, which aligns with expectations. However, no clear correlation between resonant frequency shifts and PM mass was observed. This may be due to the system operating in the transitional region between the elastic loading and resonance regimes, where frequency changes are unstable.

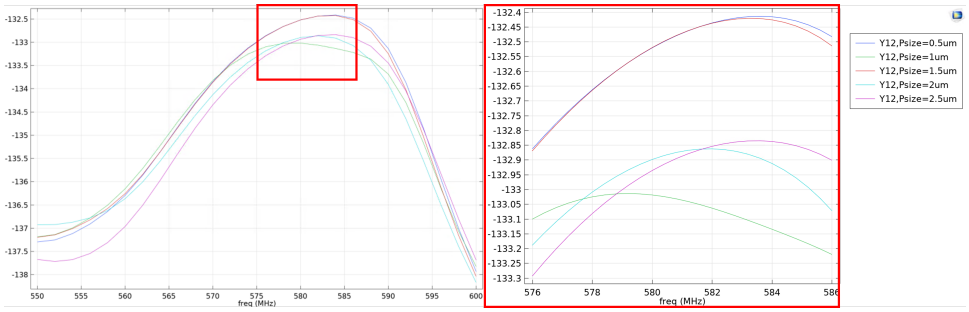

Figure 5.13: Resonant frequency with SiO2 cubic length from 0.5 μm to 2.5 μm

For SiO2 particles with resonant frequencies in breathing mode below 580 MHz, particle sizes between 9-15 μm were selected. From the simulation results shown in Figure 5.14, it is clear that the overall resonant frequencies are above 584 MHz, confirming that the particles are in the elastic loading regime. Moreover, the resonant frequencies increase as the size of the SiO2 cubic particles increases. Although the SiO2 particles and the electrode structure used in the simulation differ from the actual setup, these results effectively demonstrate that the SAW resonator has the capability to detect particle size characteristics in the elastic loading regime.

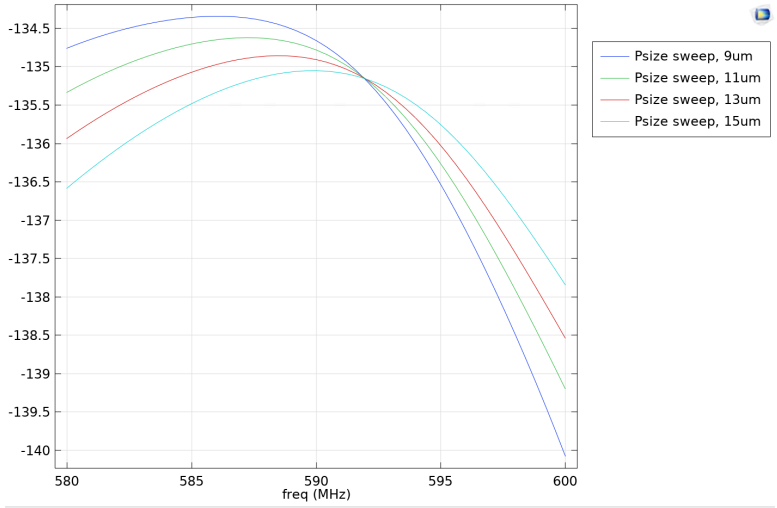

Figure 5.14: Resonant frequency with SiO2 cubic length from 9 μm to 15 μm

6

Layout Design

Based on the simulation results, the author determined the size and layout of the final designed SAW resonator device for fabrication.

6.1. SAW Resonator cross structure design

In the Mass & Elastic Region method, the resonance frequency refers to the resonance of the entire PM-SAW system. Based on the results from the particle breathing mode resonance simulation shown in Table 5.1, the elastic loading detection frequency was set at 412 MHz—significantly higher than the simulated eigenfrequency for SiO2 particles larger than 12 μm in diameter. A higher frequency was not chosen due to limitations imposed by the minimum lithographic aperture of the laser writer used in the cleanroom. To ensure a clear electrode lithography pattern, the wavelength of the SAW device must not be smaller than 12 μm, which corresponds to a resonance frequency of about 412 MHz for the AlN SAW resonator. The mass loading detection frequency, on the other hand, was set at a lower 95 MHz at the wavelength of 52 μm, below the simulated eigenfrequency for SiO2 particles smaller than 40 μm in diameter.

To achieve the purpose of detecting the PM characteristics at both high and low frequencies with same detecting area, the author designed a cross-structured SAW resonator, placing resonators with different wavelengths horizontally and vertically. The design of this cross-structured SAW resonator is shown in Figure 6.1.

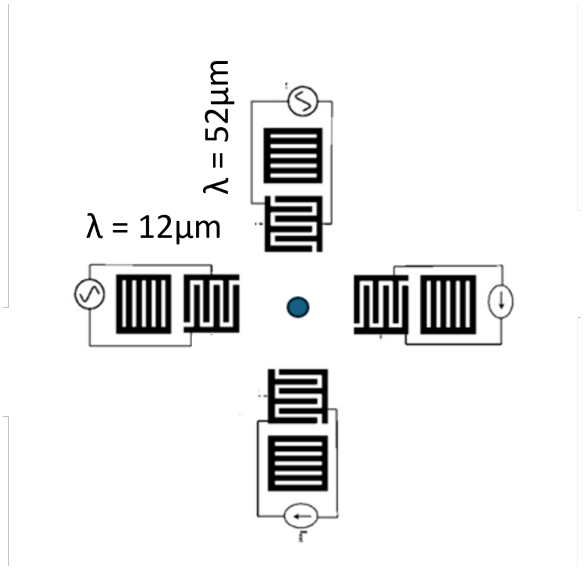

Figure 6.1: SAW Resonator cross structure design

6.2. Final device layout

The final wafer for the PM loading test was chosen to have a Reflector to IDT ratio of 1:3, with a total number of electrodes of 40 pairs and 20 pairs. And 2 more Scattering optimization designs were introduced to reduce the insertion loss. Additionally, a 40 μm diameter pad electrode was placed in the detection area to replace particle clusters. This metal pad serves as a backup in case the PM cannot be properly loaded into the detection area. The specific layout design is shown in Fig 6.2.

30 IDT 10 REF 95-412MHz	15 IDT 5 REF 95-412MHz	30 IDT 10 REF Scattering OPT 95-412MHz	15 IDT 5 REF Scattering OPT 95-412MHz
			30 IDT 10 REF Scattering OPT 95-412MHz With metal pad
30 IDT 10 REF 95-412MHz	15 IDT 5 REF 95-412MHz	30 IDT 10 REF Scattering OPT 95-412MHz	15 IDT 5 REF Scattering OPT 95-412MHz

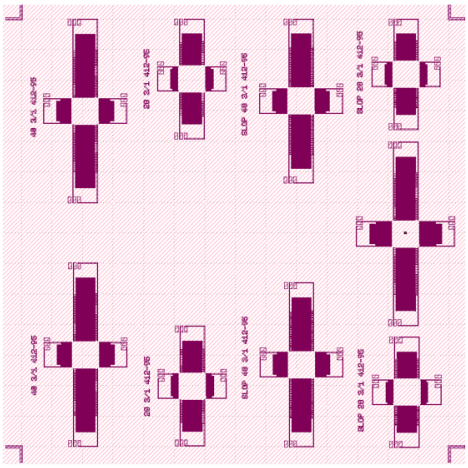

Figure 6.2: Parameters and pattern for the PM loading test

7

Fabrication

After obtaining a series of design parameters from the simulations, a detailed production plan must be developed. This section outlines the fabrication process, following the steps in the Fabrication Flowchart provided in Appendix B, conducted in the EKL cleanroom.

7.1. Fabrication process overview

To minimize electrical interference from the Si substrate, the author used a high-resistance, double-side polished Si wafer provided by the EKL cleanroom as the substrate for fabricating SAW devices. The specific parameters of the Si wafer are detailed in the table below.

Table 7.1: Parameters of the 500 nm DSP Si wafers

Type	p-doped
Orientation	$< 100 >$
Resistivity	$>$ 100 ohm-cm
Thickness	500 $\mu m \pm$ 10 μm
Diameter	100 $\mu m \pm$ 0.5 μm

The entire production process can be divided into four major steps. First, a 1 μm AlN film is deposited on one side of a cleaned Si wafer. Next, a layer of photoresist is applied to the AlN film, and the designed SAW resonator pattern is transferred via photolithography using a laser writer, followed by photoresist development. After a brief surface clean-up, metal evaporation of aluminum is performed using the CHA system. Finally, the aluminum IDTs and reflector patterns are completed through a lift-off process. A visualization of the fabrication overview is shown in Figure 7.1. The details of Fabrication are described in the following subsections.

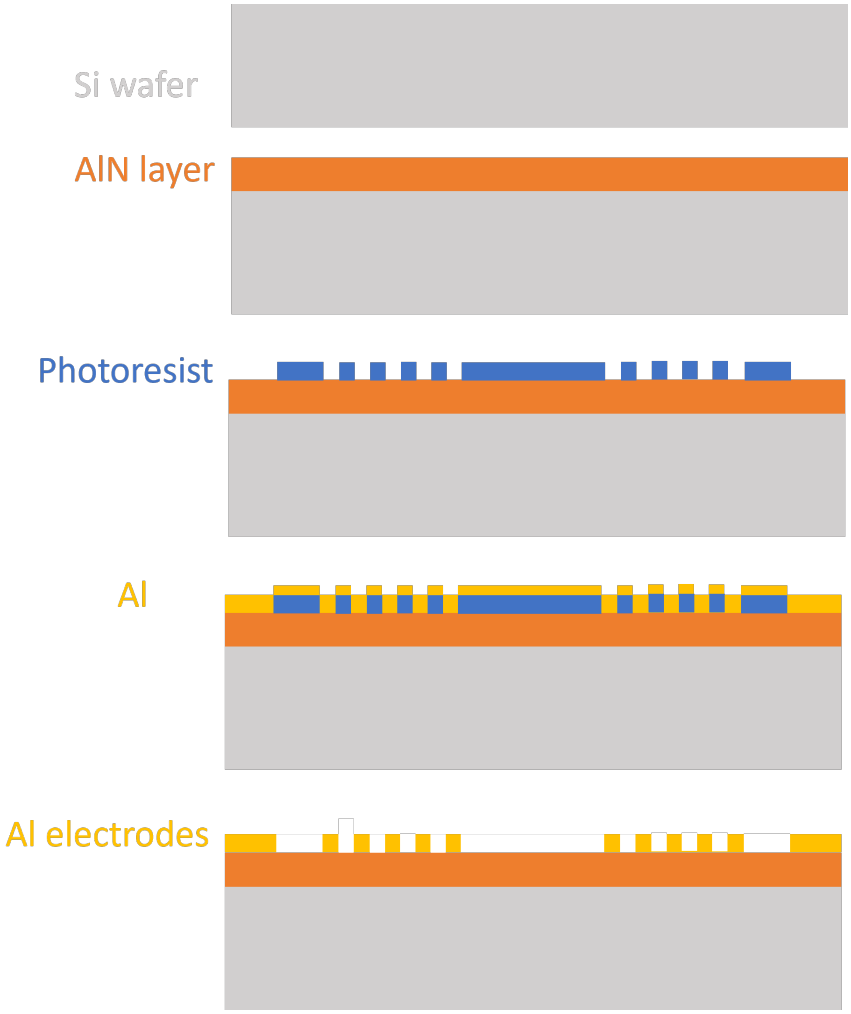

Figure 7.1: Process Overview

7.2. Deposition of AlN layer

AlN deposition was carried out using the TRIKON SIGMA DC magnetron sputtering reactor in the EKL cleanroom, following the standard 1 μm AlN recipe: AlN_1μm_400C_LS. After successfully fabricating a 1 μm AlN-deposited Si wafer, the thickness and surface flatness of the AlN layer were measured using an Ellipsometer, while X-ray Diffraction (XRD) was used to analyze the crystal structure. The Ellipsometer measurements, shown in the table below, indicate that the AlN layer thickness is close to the desired 1 μm with a relatively flat surface.

Table 7.2: AlN layer Ellipsometer measurements

AlN	893.53 nm
Rough	12.497 nm

XRD analysis was conducted at the X-RAY Facilities Group. The 1D diffraction patterns measured for the 1 μm AlN layer on a Si (001) wafer are shown in Figure 7.2.

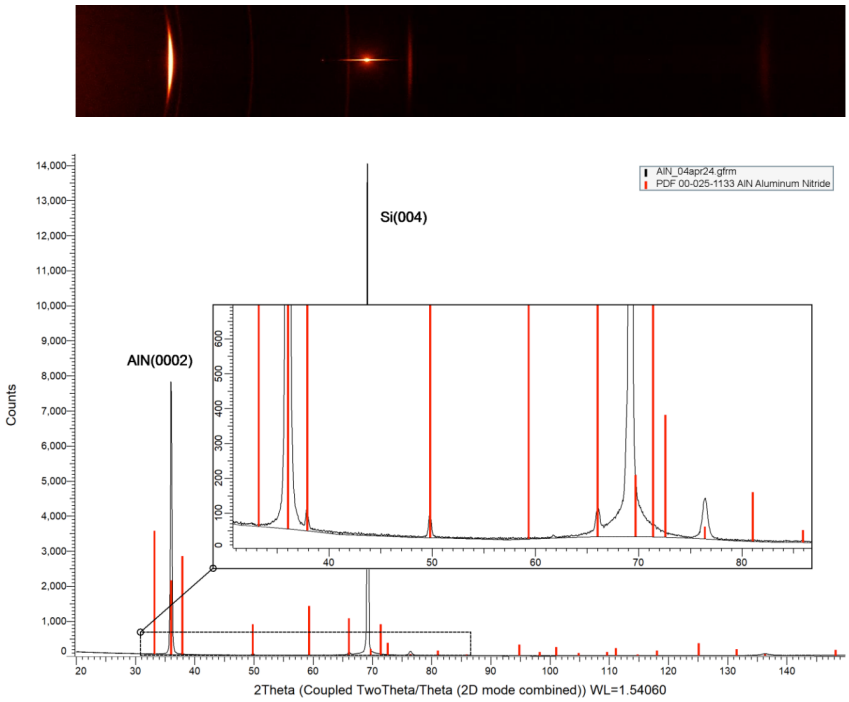

Figure 7.2: 2D and 1D XRD patterns

The figures indicate a strong preferred (0001) AlN orientation (the basal plane of the hexagonal structure), as evidenced by the prominent (0002) peak at $2\Theta = 36°$. While other planes are visible, their peaks are much weaker than anticipated. The diffraction spots around $2\Theta = 69°$ correspond to the Si(001) substrate. These results demonstrate that the standard 1 μm AlN recipe successfully produces a high-quality AlN piezoelectric layer.

7.3. Electrode lift-off

Electrode lift-off is a widely used microfabrication technique for patterning thin-film materials, such as metals, onto a substrate. While both etching and lift-off methods can be used to achieve the desired electrode pattern, selecting a suitable chemical solvent for etching the photoresist without damaging the AlN layer is particularly challenging. For this reason, the lift-off method, despite taking longer, was chosen to create the Al electrodes.

After several tests, the author identified the optimal lift-off process. The Arp5350 positive photoresist was successfully lifted off at room temperature by immersing the wafer in acetone for approximately 40 minutes. Following this, the wafer was rinsed in IPA to remove acetone residues, then in DI water to eliminate chemical solvent remnants, and finally re-immersed in IPA to facilitate quick air drying. Unlike the conventional lift-off process, an ultrasonic bath was not used to accelerate the photoresist breakdown in acetone. It was found that the Al electrodes deposited via CHA evaporation in the EKL cleanroom were easily dislodged during ultrasonic treatment, likely due to the slender dimensions of the electrodes in the design. As a result, the author opted to let the wafer rest vertically in acetone for 40 minutes, allowing the photoresist and excess Al to disintegrate and detach naturally.

Microscope comparisons of the electrode patterns before and after lift-off, as shown in Figure 7.3, reveal that the electrode width change is within 200 nm, demonstrating that this lift-off process produces high-quality Al electrodes for the SAW devices.

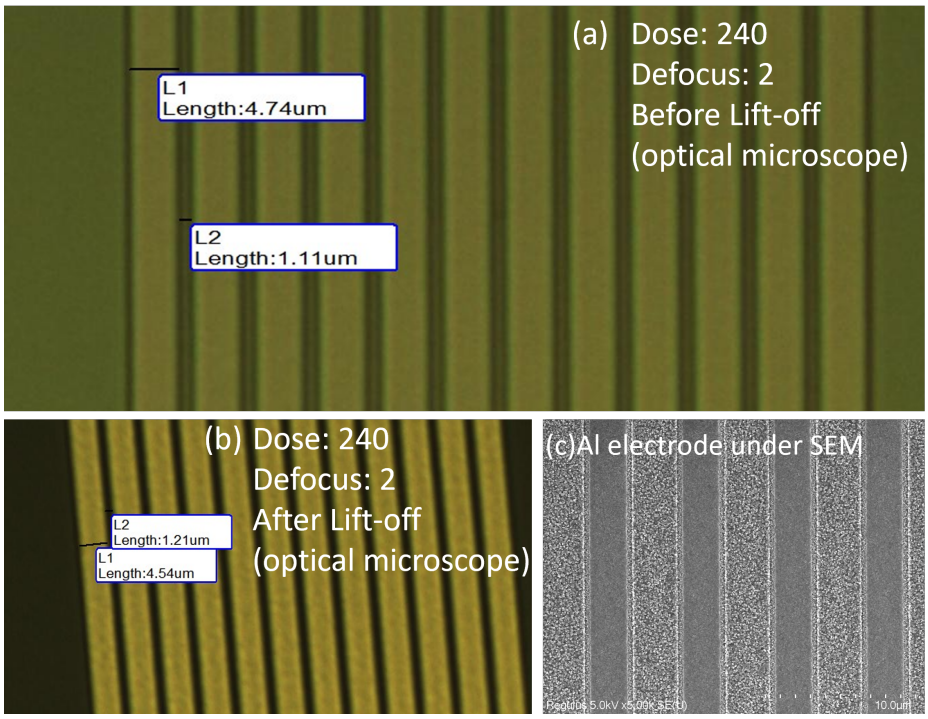

Figure 7.3: (a)Al Electrode pattern before lift-off under optical microscope, (b)Al Electrode pattern after lift-off under optical microscope, (c)Al Electrode pattern after lift-off under SEM

8

Experiment Setup

Measurements of the fabricated SAW resonators were performed after successful device fabrication. As previously mentioned, the key measurement involves detecting the change in the resonant frequency of the SAW resonator before and after contact with the PM. The resonant frequency will be determined by measuring the S-parameters of the device using a vector network analyzer (VNA). For PM, a 15 μm SiO2 particulate suspension from Microparticles GmbH was selected. Detailed instructions for using the VNA measurement platform in Earl McCune Lab can be found in Appendix C, and the product specifications for the 15 μm SiO2 particulate suspension are provided in Appendix D. This section describes the procedure for applying the 15 μm SiO2 PM to the detection area of the SAW resonator.

A small amount of PM can be transferred to the SAW resonator's measurement area using a pipette, as shown in Figure 8.1(a). However, due to the high initial concentration of the 15 μm SiO2 particulate suspension, using the original suspension directly results in excessive PM deposition, as seen in Figure 8.1(b). To address this, the suspension must first be diluted (Appendix E). After removing a portion of the suspension, it was diluted by 20x and 50x, and observed under a microscope. The results showed that the 50x dilution resulted in 0–2 particles in the detection area, while the 20x dilution resulted in 15–30 particles, as shown in Figures 8.1(c) and 8.1(d), respectively. Since an insufficient number of particles would hinder the detection of significant resonant frequency shifts, a 20x dilution was selected for PM loading.

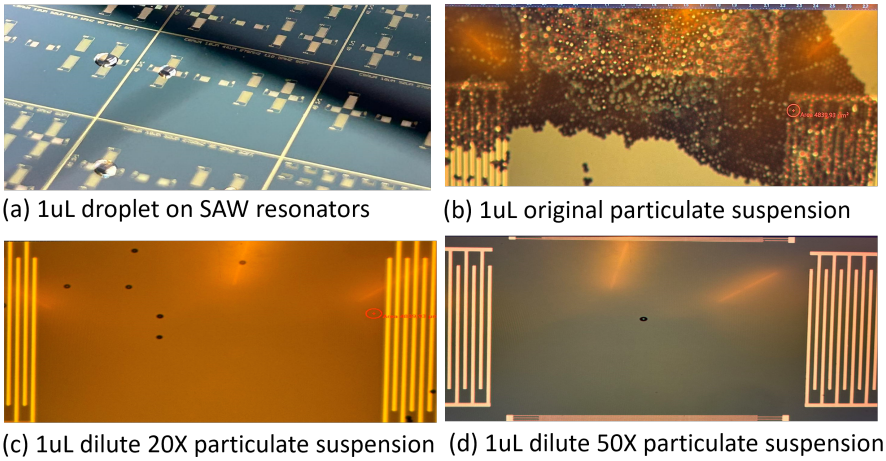
(a) 1uL droplet on SAW resonators

(b) 1uL original particulate suspension

(c) 1uL dilute 20X particulate suspension

(d) 1uL dilute 50X particulate suspension

Figure 8.1: (a) 1μm droplet on SAW resonators, (b) 1μm original particulate suspension, (c) 1μm dilute 20X particulate suspension, (d) 1μm dilute 50X particulate suspension

9

Measurement Results and Discussion

In this section, the SAW resonant frequency data measured using the VNA system will be analyzed. First, the performance of a single straight SAW resonator is compared to that of a cross-configuration SAW resonator. Next, a comparison is made between SAW resonators with various Reflector and IDT structures. Following this, the resonant frequency shifts around 412 MHz (high frequency) and 95 MHz (low frequency) before and after PM loading are evaluated and compared.

9.1. Cross & Single Structure

As outlined in the Layout Design section, a cross-structured SAW resonator was developed, featuring a 412 MHz high-frequency two-port SAW resonator positioned horizontally and a 95 MHz low-frequency two-port SAW resonator placed vertically. This configuration is designed to detect PM characteristics at both high and low frequencies within the same detection area.

Theoretically, the aperture number in the SAW resonator design is significantly larger than the wavelength, meaning the IDT boundary in the detection region of the cross-structure SAW resonator should not interfere with Rayleigh wave transmission. To validate this, measurement results of the 95.2 MHz SAW resonator in the cross structure and the single straight 95.2 MHz SAW resonator (both without PM loading) were compared on the same wafer. The results are shown in Fig 9.1(a) and Fig 9.1(b), respectively. A similar comparison for the 412 MHz SAW resonators is presented in Figure 9.2.

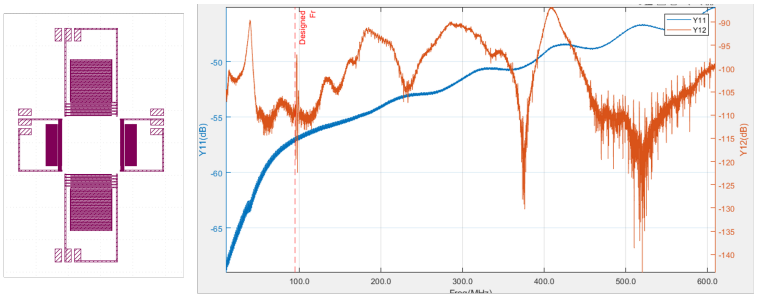

(a) Single straight SAW resonator with 95.2MHz designed Fr

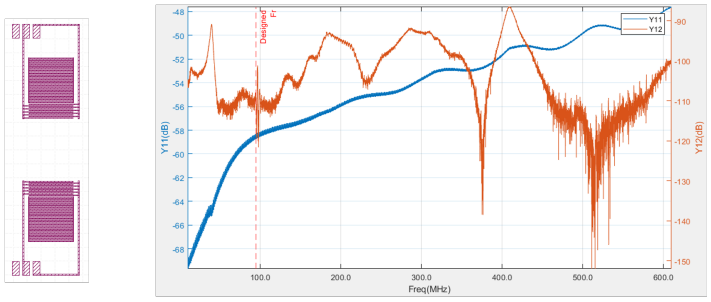

(b) Cross structure SAW resonator with 95.2MHz designed Fr

Figure 9.1: (a) Cross structure SAW resonator with 95.2MHz designed Fr, (b) Single straight SAW resonator with 95.2MHz designed Fr

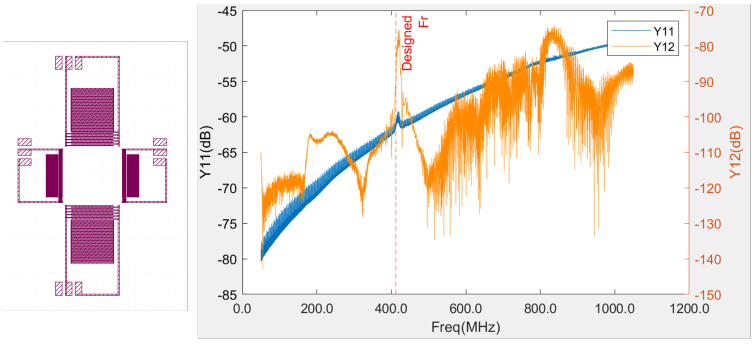

(a) Cross structure SAW resonator with 412MHz designed Fr

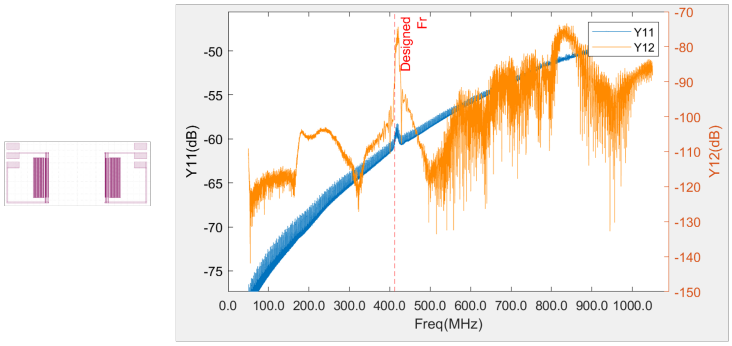

(b) Single straight SAW resonator with 412MHz designed Fr

Figure 9.2: (a) Cross structure SAW resonator with 412 MHz designed Fr, (b) Single straight SAW resonator with 412 MHz designed Fr

Measurements reveal resonances at frequencies other than the designed 95 MHz, a pattern observed across several batches of devices. This additional resonance is likely caused by environment noise

from the VNA probe station. Nonetheless, the comparison of the two figures clearly shows that the use of the cross structure does not introduce any significant shift in the measured resonant frequencies. This confirms that any shifts observed in subsequent measurements are primarily due to changes in the contact state within the detection area.

9.2. Fabricated SAW resonators with different Reflectors & IDTs Structures

Based on the simulation results of the electrode structure in Section 5.6, a series of devices with varying IDT/Reflector ratios and different total numbers of IDTs and reflectors were fabricated for comparison. The device operating at 275 MHz and 412 MHz, which showed superior fabrication quality compared to the others, was selected for detailed analysis. The results are presented in Figure 9.3.

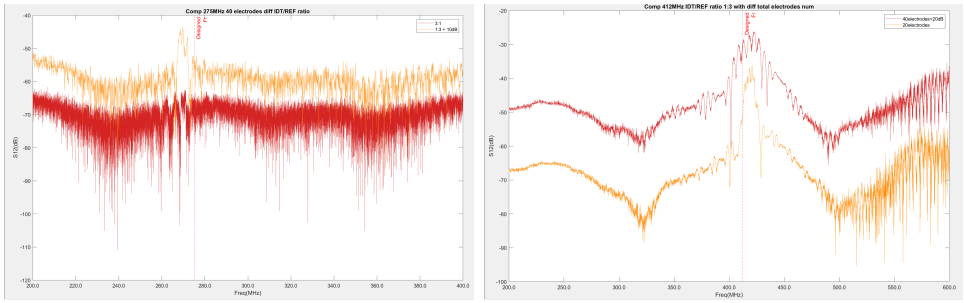

(a) 275MHz, 40 total IDT&REF, changing IDT/REF ratio of 3:1 and 1:3

(b) 275MHz, IDT/REF ratio of 1:3, changing total IDT&REF of 20 and 40

Figure 9.3: (a) 275MHz, 40 total IDT&REF, changing IDT/REF ratio of 3:1 and 1:3, (b) 412MHz, IDT/REF ratio of 1:3, changing total IDT&REF of 20 and 40

In Figure 9.3(a), with the total number of IDTs and reflectors fixed at 40, the 1:3 IDT-to-reflector ratio shows a more pronounced resonance around 275 MHz compared to the 3:1 ratio. In Figure 9.3(b), when the IDT-to-reflector ratio is held at 1:3 but the total number of reflectors is increased, the issue of multiresonance becomes more pronounced. These results further confirm the pattern observed in the simulations discussed in Section 5.6.

9.3. 15 μm SiO2 PM cluster loading

The initial cross-SAW resonant frequency was benchmarked without PM loading. After diluting the particulate suspension as outlined in the Experimental Setup, PM was applied using a pipette, and the suspension was allowed to dry naturally. The distribution of PM clusters was observed under an optical microscope, as shown in Fig 9.4. While some PM was successfully loaded in the detection area (Fig 9.4(a)), the drying process left noticeable liquid stains, a problem evident in all the figures. Notably, no PM loading was observed in Fig 9.4(d). In Fig 9.4(c), part of the PM cluster is located in the upper right corner of the detection area, and the liquid staining is less pronounced compared to Fig 9.4(a). Therefore, the focus during the measurement process was on the results from Fig 9.4(c).

Figure 9.4: (a) PM loading on 30 IDT, 10 REF, 95-412MHz, (b) PM loading on 15 IDT, 5 REF, 95-412MHz, (c) PM loading on 30 IDT 10 REF Scattering OPT 95-412MHz, (d) PM loading on 15 IDT 5 REF Scattering OPT 95-412MHz

The S-parameter measurement results at 95 MHz (low frequency) and 412 MHz (high frequency) are shown in Fig. 9.5 and Fig. 9.6, respectively. Even in the 30 IDT 10 REF Scattering OPT 95-412 MHz device, which had better PM loading results (Fig. 9.4(c)), no significant resonance frequency variations were detected at either low or high frequencies. This outcome was consistent across other devices with less optimal PM loading conditions.

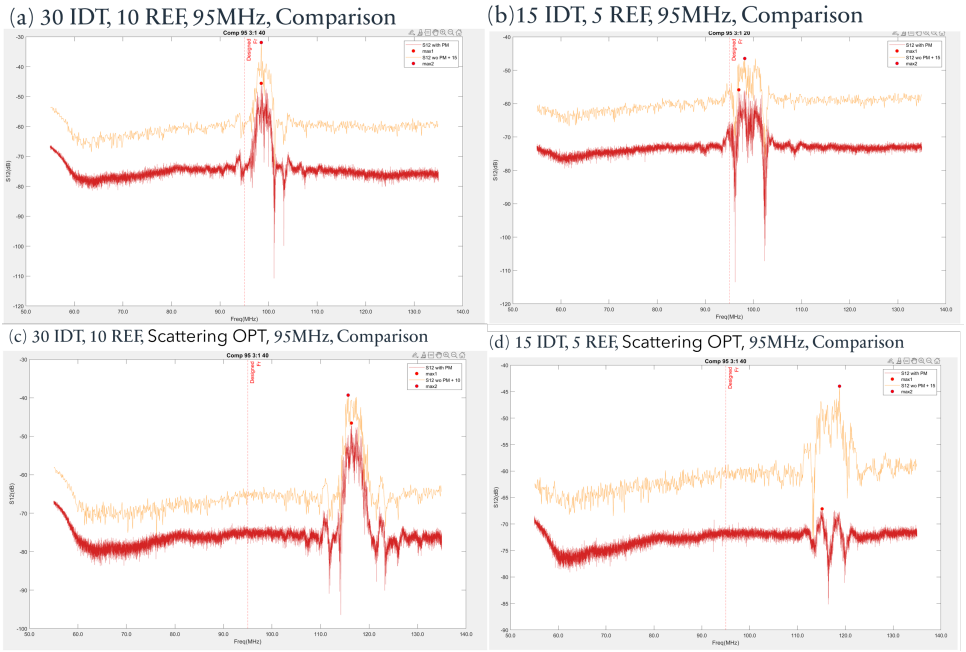

Figure 9.5: (a) Comparison of 30 IDT 10 REF 95MHz, (b) Comparison of 15 IDT 5 REF 95MHz, (c) Comparison of 30 IDT 10 REF Scattering OPT 95MHz, (d) Comparison of 15 IDT 5 REF Scattering OPT 95MHz

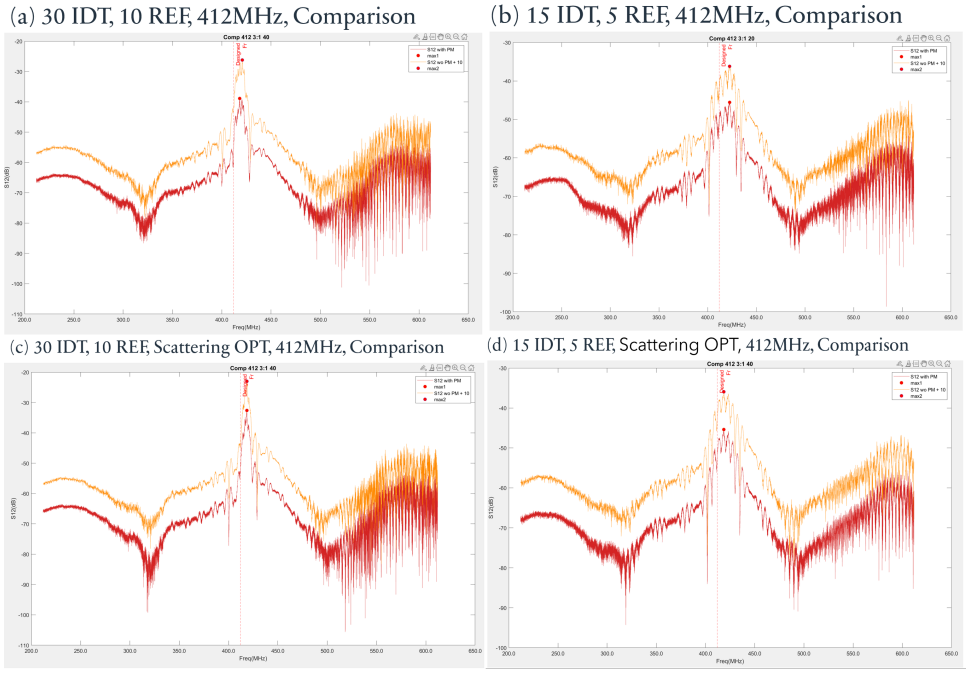

Figure 9.6: (a) Comparison of 30 IDT 10 REF 412MHz, (b) Comparison of 15 IDT 5 REF 412MHz, (c) Comparison of 30 IDT 10 REF Scattering OPT 412MHz, (d) Comparison of 15 IDT 5 REF Scattering OPT 412MHz

9.4. Al column loading

To determine whether the absence of a significant resonant frequency shift after PM loading was due to a malfunction in the fabrication of the SAW device, the author measured the devices outlined in the Layout Design section using a metal pad in place of particles.

The results revealed a significant resonance shift was observed in the device using 40 μm diameter and 200 nm height column Al electrode instead of PM loading, as shown in Fig. 9.7. Specifically, at low frequencies around 95 MHz, a negative resonance frequency shift of approximately -20 MHz was detected (shown in 9.7(b)), while at high frequencies around 412 MHz, a negative shift of about -180 MHz was observed (shown in 9.7(a)). The measurements with Al pad loading and PM loading are analyzed below.

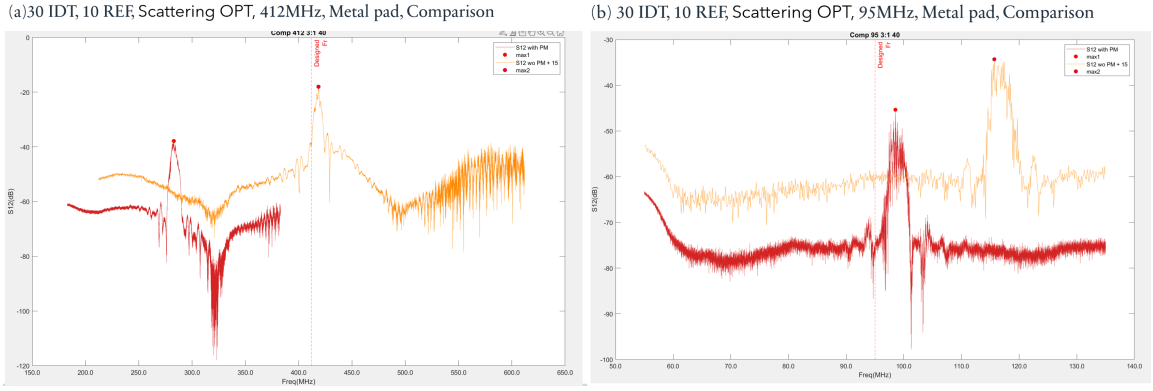

Figure 9.7: (a) Comparison of 30 IDT 10 REF Scattering OPT 412MHz with 40 μm metal pad, (d) Comparison of 30 IDT 10 REF Scattering OPT 95MHz with 40 μm metal pad

Firstly, the observation of varying magnitudes of frequency shifts at both low and high frequencies in devices using metal pads indicates that the fabricated cross-structure 95-412 MHz SAW resonator is

capable of detecting mass characteristic in its surface detection region effectively. Additionally, the device parameters are consistent with those used for PM loading with actual SiO2 particles. The mass of a single 15 μm SiO2 particle (approximate $4.68 \times 10^{-9} g$) is significantly larger than that of a 200 nm high column Al electrode with a 40 μm diameter($6.81 \times 10^{-10} g$). Therefore, the mass loading detection region in Fig. 9.4 has already reached a detectable range.

It is reasonable to assume that the inability to detect frequency shifts with PM loading of actual SiO2 particles is primarily due to water residue on the SAW detection area, which affects the contact between the particles and the AlN surface. Under normal conditions, as shown in Figure 9.8, the contact between the particles and the sensor surface can be described as follows:

- For low-frequency vibrations in the mass-loading regime, the particle adheres almost rigidly to the sensor surface, moving in-phase with the interface. This means the particle moves harmonically around the equilibrium position, effectively vibrating with the surface.
- For high-frequency vibrations in the elastic-loading regime, the particle is weakly coupled to the sensor surface through soft stiffness. The stress is concentrated near the contact interface, while the main body of the particle remains relatively stationary, as if clamped by the sensor surface.

However, the presence of liquid stains with unknown properties disrupts this vibrational pattern. Consequently, the expected frequency shift cannot be detected due to the interference caused by these stains.

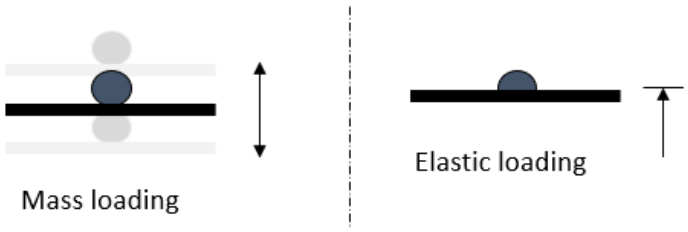

Figure 9.8: Schematic diagram of the contact between the particles and the surface of the SAW detection area

The measurements of the 40 µm column electrode, which show a negative frequency shift increasing with detection frequency (Figure 9.7), are analyzed in conjunction with the frequency changes across different regimes (Figure 3.2). This analysis aligns with the mass loading regime depicted in Figure 3.2. It can be deduced that the mass loading regime has not been exceeded, even at the 412 MHz SAW resonance frequency.

10

Conclusion

The primary research question of this project is: How can a SAW device be engineered to concurrently measure both the mass and elastic characteristics of individual particulate matters attached to it? To address this question, the author refers to the Mass and Elastic Region Method proposed by Yang and aims to measure frequency shifts before and after PM loading at both low and high frequencies for SAW surfaces in contact with PM, to investigate characteristics under different regimes.

Firstly, the author estimates the required low and high frequency values by simulating the eigenfrequencies of SiO2 particles in their breathing mode. Simulations of the effects of AlN layer thickness and the choice of Au and Al electrode materials on SAW resonator performance then inform the selection of materials and parameters for actual fabrication. The electrode patterns are determined by simulating the IDT and reflector designs. Additionally, scattering optimization is employed to reduce insertion loss by refining the IDT and reflector patterns. The final fabrication decision includes 30 pairs of IDTs and 10 pairs of reflectors with and without scattering optimization at 95 MHz and 412 MHz; and 15 pairs of IDTs and 5 pairs of reflectors with and without scattering optimization at these frequencies.

Following training in the Else Kooi Lab cleanroom and consultations with relevant staff, a specific fabrication flowchart was developed. The SAW resonator produced successfully provided the required resonance frequencies as measured by the VNA probe station. The SiO2 particulate suspension was diluted and applied to the device's detection area for measurement after PM loading. As discussed in Section 9, Measurement Results, no significant resonance frequency changes were observed from the actual PM loading measurements. Instead, a notable negative frequency shift was detected under mass loading conditions with aluminium column, rather than with SiO2 particles. This suggests that water residue from the suspension during PM loading disrupts the direct contact between the PM and the detecting area surface, preventing accurate detection of surface perturbations in both mass and elastic loading regimes.

In summary, the cross-structure 95 MHz and 412 MHz SAW resonator, fabricated following the process outlined in Appendix B, effectively detects mass loading characteristics with a 40 μm diameter, 200 nm high aluminum column in the detection area. Additionally, based on the 3D simulations discussed in Section 5.8, the resonator shows significant potential for detecting both mass and elastic properties of PM, provided that any water residues in the suspension are removed.

11

Reflection and Recommendation

The cross-structure 95 MHz and 412 MHz SAW resonators, utilizing AlN as the piezoelectric layer, were fabricated to assess their sensitivity to 15 μm diameter SiO2 particles. However, no significant frequency shift was detected following PM loading. After reflecting on the simulation, fabrication, and measurement phases of the project, this section summarizes key insights and offers recommendations for future development.

11.1. PM contact simulation

As discussed in Section 5.8, the author explored in simulations whether introducing additional contact on the surface of the SAW resonator affected its performance by manipulating the mass of the SiO2 cube, setting it to zero or not. However, the results showed that even when the mass of the SiO2 cube was set to zero, it still perturbed the mode shape of the system. This may be due to the space occupied by the SiO2 cube in the COMSOL model exerting some damping effect on the surface of the SAW resonator. To more accurately simulate the SAW resonator's vibration modes, it would be more effective to create a model in which the SiO2 cubes are completely removed.

Additionally, the meshing setup in COMSOL for the SiO2 cube on the SAW resonator surface warrants further reflection. As shown in Figure 11.1, a triangular mesh was applied to the sides of the SiO2 cube and the detection area of the SAW resonator to accelerate the 3D simulation. However, this approach may have compromised precision, potentially explaining the lack of correlation between resonant frequency and SiO2 cube size observed in Figure 5.13. To more effectively simulate vibration mode changes due to cubic PM contact, it might be beneficial to reduce mesh elements on the SAW resonator side and apply a finer mesh at the intersection of the cube and probe area, without significantly increasing simulation time.

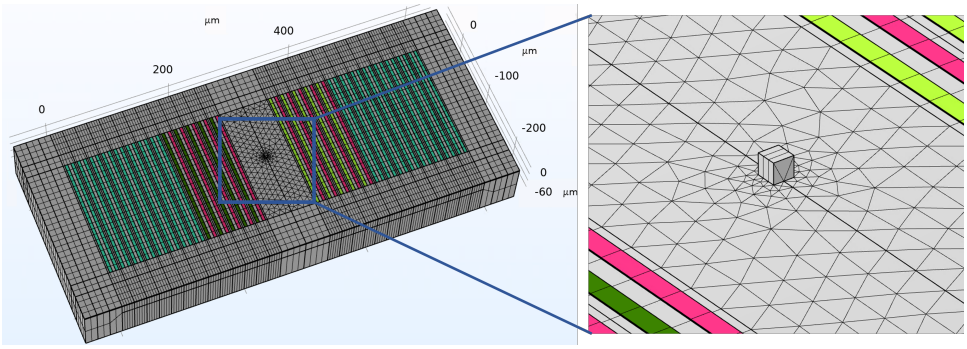

Figure 11.1: Schematic diagram of the COMSOL meshing on SAWR SiO2 cubic

Two meshing methods, Free Triangular and Mapped, were applied to the cubic particle and SAW cavity (i.e., the detection area) to optimize the simulation. The aim was to reduce the lateral simulation elements for the SAW while increasing the vertical elements for the cubic particle. The mesh configurations are shown in Figure 11.2.

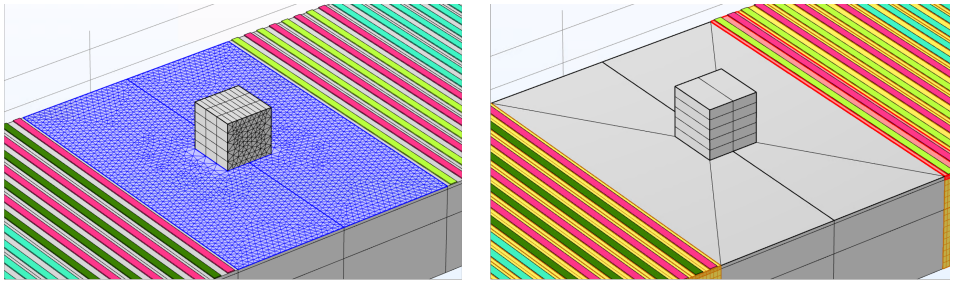

(a) Free Triangular Meshing (b) Mapped Meshing

Figure 11.2: (a) Free Triangular Meshing, (b) Mapped Meshing

In the Free Triangular method (Figure 11.2(a)), COMSOL enforces continuous triangular meshing patterns between the edges of the cubic particle and the SAW cavity. This results in a large number of elements between the cubic edge and the detection area, limiting the ability to further reduce lateral elements.

In contrast, the Mapped method (Figure 11.2(b)) divides the SAW cavity into just six elements. However, using too few elements risks distorting the simulation results. Additionally, when sweeping the cubic particle size, the mesh settings do not automatically adjust in Mapped meshing. This requires manually configuring the mesh for each cubic size, which can be time consuming. More advanced meshing techniques could potentially offer better efficiency and accuracy for future simulations.

11.2. IDT and Reflector fabrication

As mentioned earlier in Section 5.4, aluminium was chosen for the fabrication of both the IDTs and reflectors to achieve higher resonant frequencies. Theoretically, the resonance frequency is primarily determined by the IDT, while the use of denser metals can enhance the performance of the reflectors. Therefore, it might be possible to further improve device performance by using different materials for the electrodes, such as aluminium for the IDT and gold for the reflectors. Fabricating electrodes from different materials can be achieved through sequential metal evaporation, with photolithography applied to the IDTs and reflectors in two separate steps using a laser writer.

11.3. Removal of liquid stains

The inability to detect frequency shifts during PM loading with actual SiO2 particles is primarily attributed to liquid stains on the SAW detection area. The presence of residues, aside from the particles being measured, directly affects the accuracy of the results.

Upon identifying this issue, the author attempted to remove the liquid stains using chemical reagents. First, the PM-loaded device was immersed in acetone and left to stand, followed by immersion in IPA to wash off any residual chemicals before air drying. However, as shown in Fig 11.3(a), the stains were not effectively removed from the SAW resonator's detection area. Next, the same cleaning procedure was repeated with the addition of a low-power ultrasonic bath, which led to partial removal of the stains, as seen in Fig 11.3(b). This suggests that liquid stains can be reduced by cleaning the SAW detection area with chemical reagents after PM loading via pipette.

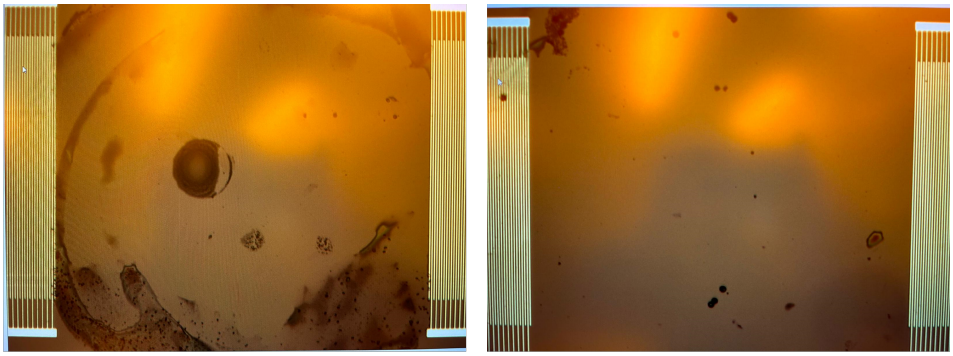

(a) After chemical cleaning

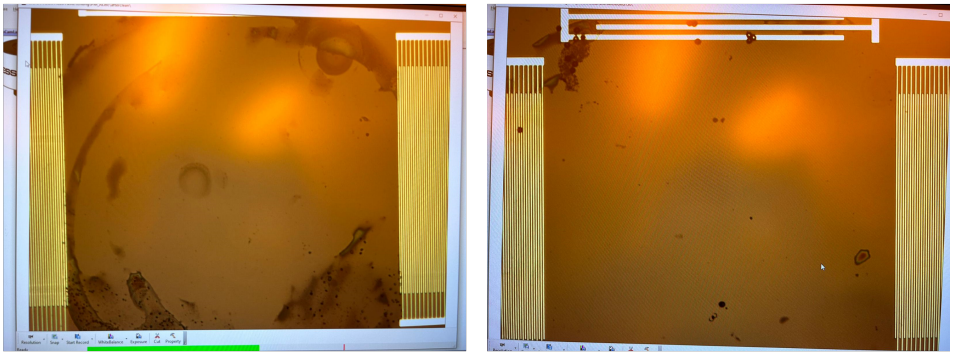

(b) After chemical cleaning with ultrasound bath

Figure 11.3: PM loading devices (a) after chemical cleaning, (b) after chemical cleaning with ultrasound bath

Improving PM contact can be achieved by addressing the issue of liquid stains, and several potential sources of these stains have been identified. First, after diluting the initial 15 μm SiO2 suspension, the solution was stored in self-contained glassware, which may not have been as airtight as the original packaging. This could have allowed impurities to enter during storage, negatively impacting the effectiveness of PM loading. To mitigate this, it is recommended that PM loading be performed immediately after diluting the SiO2 suspension to improve contact quality. Second, liquid stains could have originated from contamination of pipettes or other tools used in the PM loading process. Therefore, all equipment involved in PM loading should be thoroughly cleaned before use. Additionally, slightly increasing the temperature during the drying process, while ensuring a clean, dry, and well-ventilated environment, may further help prevent the formation of liquid stains.

References

[1] J. Dong et al. “Particulate matter”. In: *Handbook on Characterization of Biomass, Biowaste and Related by-Products* (2020), pp. 1267–1306. DOI: 10.1007/978-3-030-35020-8_14.

[2] M. Politis et al. “ULTRAFINE PARTICLES (UFP) AND HEALTH EFFECTS. DANGEROUS. LIKE NO OTHER PM? REVIEW AND ANALYSIS”. English. In: *Global nest journal* 10.3 (Nov. 2008), pp. 439–452. ISSN: 1790-7632.

[3] Katalin Hubai, Nora Kováts, and Gábor Teke. “Effects of urban atmospheric particulate matter on higher plants using Lycopersicon esculentum as model species”. In: *SN Applied Sciences* 3.9 (2021), pp. 2523–3971. DOI: 10.1007/s42452-021-04745-8.

[4] Yong-Keun Choi et al. “Morphological and Chemical Evaluations of Leaf Surface on Particulate Matter2.5 (PM2.5) Removal in a Botanical Plant-Based Biofilter System”. In: *Plants* 10.12 (2021). ISSN: 2223-7747. DOI: 10.3390/plants10122761. URL: https://www.mdpi.com/2223-7747/10/12/2761.

[5] Evangelia E. Golia. “The impact of heavy metal contamination on soil quality and plant nutrition. Sustainable management of moderate contaminated agricultural and urban soils, using low cost materials and promoting circular economy”. In: *Sustainable Chemistry and Pharmacy* 33 (2023), p. 101046. ISSN: 2352-5541. DOI: https://doi.org/10.1016/j.scp.2023.101046. URL: https://www.sciencedirect.com/science/article/pii/S2352554123000803.

[6] Shau-Liang Chen et al. “Possible warming effect of fine particulate matter in the atmosphere”. In: *Communications Earth Environment* 2 (2021), p. 208. ISSN: 2662-4435. DOI: https://doi.org/10.1038/s43247-021-00278-5. URL: https://www-nature-com.tudelft.idm.oclc.org/articles/s43247-021-00278-5#citeas.

[7] L. Yang, L. Cheng, and X. Tang. “The impact of pm2.5 on the host defense of respiratory system”. In: *Frontiers in Cell and Developmental Biology* 8 (2020). DOI: 10.3389/fcell.2020.00091.

[8] Q. Wang and S. Li. “The effects and pathogenesis of pm2.5 and its components on chronic obstructive pulmonary disease”. In: *International Journal of Chronic Obstructive Pulmonary Disease* Volume 18 (2023), pp. 493–506. DOI: 10.2147/copd.s402122.

[9] C. Krittanawong et al. “Pm2.5 and cardiovascular health risks”. In: *Current Problems in Cardiology* 48 (6 2023), p. 101670. DOI: 10.1016/j.cpcardiol.2023.101670.

[10] A. Yang et al. “Global premature mortality by dust and pollution pm2.5 estimated from aerosol reanalysis of the modern-era retrospective analysis for research and applications, version 2”. In: *Frontiers in Environmental Science* 10 (2022). DOI: 10.3389/fenvs.2022.975755.

[11] S. Kim et al. “Air pollution and central nervous system disease: a review of the impact of fine particulate matter on neurological disorders”. In: *Frontiers in Public Health* 8 (2020). DOI: 10.3389/fpubh.2020.575330.

[12] D. Schweizer, R. Cisneros, and G. D. Shaw. “A comparative analysis of temporary and permanent beta attenuation monitors: the importance of understanding data and equipment limitations when creating pm 2.5 air quality health advisories”. In: *Atmospheric Pollution Research* 7 (5 2016), pp. 865–875. DOI: 10.1016/j.apr.2016.02.003.

[13] J. Volckens and T. M. Peters. “Counting and particle transmission efficiency of the aerodynamic particle sizer”. In: *Journal of Aerosol Science* 36 (12 2005), pp. 1400–1408. DOI: 10.1016/j.jaerosci.2005.03.009.

[14] K. Shukla and S. G. Aggarwal. “A technical overview on beta-attenuation method for the monitoring of particulate matter in ambient air”. In: *Aerosol and Air Quality Research* 22 (12 2022), p. 220195. DOI: 10.4209/aaqr.220195.

[15] “Model 3321 Aerodynamic Particle Sizer® Spectrometer-Instruction Manual”. In: (2004). DOI: https://downloads.psl.noaa.gov/psd3/cruises/CAPRICORN_2016/Investigator/CAPRICORN/CAPRICORN_Aerosols/Manuals/APS%203321%20manual.pdf.

[16] A. Wajid. “On the accuracy of the quartz-crystal microbalance (qcm) in thin-film depositions”. In: *Sensors and Actuators A: Physical* 63 (1 1997), pp. 41–46. DOI: 10.1016/s0924-4247(97)80427-x.

[17] K. Kaur et al. “Application of a quartz crystal microbalance to measure the mass concentration of combustion particle suspensions”. In: *Journal of Aerosol Science* 137 (2019), p. 105445. DOI: 10.1016/j.jaerosci.2019.105445.

[18] M. H. Eslami and N. Alizadeh. “Ultrasensitive and selective qcm sensor for detection of trace amounts of nitroexplosive vapors in ambient air based on polypyrrole—bromophenol blue nanostructure”. In: *Sensors and Actuators B: Chemical* 278 (2019), pp. 55–63. DOI: 10.1016/j.snb.2018.09.060.

[19] P. R. Reddy and B. Mohan. “Design and analysis of film bulk acoustic resonator (fbar) filter for rf applications”. In: *International Journal of Engineering Business Management* 4 (2012), p. 28. DOI: 10.5772/54921.

[20] A. Mujahid, A. Afzal, and F. L. Dickert. “An overview of high frequency acoustic sensors—qcms, saws and fbars—chemical and biochemical applications”. In: *Sensors* 19 (20 2019), p. 4395. DOI: 10.3390/s19204395.

[21] Arief Yuwono and Peter Schulze Lammers. “Odor Pollution in the Environment and the Detection Instrumentation”. In: 6 (Nov. 2003).

[22] Humberto Campanella et al. “Analytical and Finite-Element Modeling of a Localized-Mass Sensor”. In: *Proceedings of IEEE Sensors* (Oct. 2008), pp. 367–370. DOI: 10.1109/ICSENS.2008.4716457.

[23] Lord Rayleigh. “On waves propagated along the plane surface of an elastic solid”. In: *Proceedings of the London mathematical Society* 1.1 (1885), pp. 4–11.

[24] A. Khan et al. “Piezoelectric thin films: an integrated review of transducers and energy harvesting”. In: *Smart Materials and Structures* 25 (5 2016), p. 053002. DOI: 10.1088/0964-1726/25/5/053002.

[25] Changjian Zhou et al. “Temperature-Compensated High-Frequency Surface Acoustic Wave Device”. In: *IEEE Electron Device Letters* 34.12 (2013), pp. 1572–1574. DOI: 10.1109/LED.2013.2283305.

[26] A. Afzal et al. “Advanced vapor recognition materials for selective and fast responsive surface acoustic wave sensors: a review”. In: *Analytica Chimica Acta* 787 (2013), pp. 36–49. DOI: 10.1016/j.aca.2013.05.005.

[27] B. P. Bastakoti, N. L. Torad, and Y. Yamauchi. “Polymeric micelle assembly for the direct synthesis of platinum-decorated mesoporous tio2 toward highly selective sensing of acetaldehyde”. In: *ACS Applied Materials Amp; Interfaces* 6 (2 2013), pp. 854–860. DOI: 10.1021/am4039954.

[28] M. Nagaraju et al. “A fully integrated wafer-scale sub-mmlt;supgt;3lt;/supgt; fbar-based wireless mass sensor”. In: *2014 IEEE International Frequency Control Symposium (FCS)* (2014). DOI: 10.1109/fcs.2014.6859916.

[29] L. Mai et al. “A feasibility study of zno□based fbar devices for an ultra□mass□sensitive sensor application”. In: *Microwave and Optical Technology Letters* 42 (6 2004), pp. 505–507. DOI: 10.1002/mop.20351.

[30] D. R. Morris et al. “Real-time monitoring of airborne cat allergen using a qcm-based immunosensor”. In: *Sensors and Actuators B: Chemical* 190 (2014), pp. 851–857. DOI: 10.1016/j.snb.2013.09.061.

[31] A. Tarnapolsky and V. Freger. “Modeling qcm-d response to deposition and attachment of microparticles and living cells”. In: *Analytical Chemistry* 90 (23 2018), pp. 13960–13968. DOI: 10.1021/acs.analchem.8b03411.

[32] A. Budianto et al. “A study of the correlation between fine particle mass loading effect and frequency shift of a bare qcm”. In: *International Conference on Science and Applied Science (Icsas2020)* (2020). DOI: 10.1063/5.0030820.

[33] Y. Wang et al. “An aerosol sensor for pm1 concentration detection based on 3d printed virtual impactor and saw sensor”. In: *Sensors and Actuators A: Physical* 288 (2019), pp. 67–74. DOI: 10.1016/j.sna.2019.01.013.

[34] K. Lee and Y. Kim. “Portable multilateral measurement system employing optical particle counter and one-stage quartz crystal microbalance to measure pm10”. In: *Sensors and Actuators A: Physical* 333 (2022), p. 113272. DOI: 10.1016/j.sna.2021.113272.

[35] J. Specht et al. “Aln fbar particle sensor with a thermophoretic sampling mechanism”. In: *IEEE Sensors Journal* 21 (17 2021), pp. 19427–19435. DOI: 10.1109/jsen.2021.3086528.

[36] S. Thomas et al. “High frequency surface acoustic wave resonator-based sensor for particulate matter detection”. In: *Sensors and Actuators A: Physical* 244 (2016), pp. 138–145. DOI: 10.1016/j.sna.2016.04.003.

[37] L. Djoumi, M. Vanotti, and V. Blondeau-Pâtissier. “Real time cascade impactor based on surface acoustic wave delay lines for pm10 and pm2.5 mass concentration measurement”. In: *Sensors* 18 (1 2018), p. 255. DOI: 10.3390/s18010255.

[38] T. E. Angel et al. “Mass spectrometry-based proteomics: existing capabilities and future directions”. In: *Chemical Society Reviews* 41 (10 2012), p. 3912. DOI: 10.1039/c2cs15331a.

[39] Ó. Malvar et al. “Mass and stiffness spectrometry of nanoparticles and whole intact bacteria by multimode nanomechanical resonators”. In: *Nature Communications* 7 (1 2016). DOI: 10.1038/ncomms13452.

[40] A. Naik et al. “Towards single-molecule nanomechanical mass spectrometry”. In: *Nature Nanotechnology* 4 (7 2009), pp. 445–450. DOI: 10.1038/nnano.2009.152.

[41] C. March et al. “High-frequency phase shift measurement greatly enhances the sensitivity of qcm immunosensors”. In: *Biosensors and Bioelectronics* 65 (2015), pp. 1–8. DOI: 10.1016/j.bios.2014.10.001.

[42] L. Qin et al. “Characterization of polymer nanocomposite films using quartz thickness shear mode (tsm) acoustic wave sensor”. In: *Sensors and Actuators A: Physical* 136 (1 2007), pp. 111–117. DOI: 10.1016/j.sna.2006.12.027.

[43] N. I. M. Nor et al. “Film bulk acoustic wave resonator in 10–20 ghz frequency range”. In: *2016 3rd International Conference on Electronic Design (ICED)* (2016). DOI: 10.1109/iced.2016.7804692.

[44] N. Smagin et al. “Electrical and optical characterization of saw sensors coated with parylene c and their analysis using the coupling-of-modes (com) theory”. In: *Sensors* 22 (22 2022), p. 8611. DOI: 10.3390/s22228611.

[45] Günter Sauerbrey. “Verwendung von Schwingquarzen zur Wägung dünner Schichten und zur Mikrowägung”. In: *Zeitschrift für Physik* 155 (2 1959). DOI: 10.1007/BF01337937.

[46] Y. Wang et al. “A miniature system for separation and detection of pm based on 3-d printed virtual impactor and qcm sensor”. In: *IEEE Sensors Journal* 18 (15 2018), pp. 6130–6137. DOI: 10.1109/jsen.2018.2844876.

[47] S. Thomas et al. “Dual high-frequency surface acoustic wave resonator for ultrafine particle sensing”. In: *2013 Ieee Sensors* (2013). DOI: 10.1109/icsens.2013.6688319.

[48] J. Black et al. “6d-2 mems-enabled miniaturized particulate matter monitor employing 1.6 ghz aluminum nitride thin-film bulk acoustic wave resonator (fbar) and thermophoretic precipitator”. In: *2007 IEEE Ultrasonics Symposium Proceedings* (2007). DOI: 10.1109/ultsym.2007.128.

[49] M. Rodahl et al. “Quartz crystal microbalance setup for frequency and q-factor measurements in gaseous and liquid environments”. In: *Review of Scientific Instruments* 66 (7 1995), pp. 3924–3930. DOI: 10.1063/1.1145396.

[50] W. Xu et al. “A high-quality-factor film bulk acoustic resonator in liquid for biosensing applications”. In: *Journal of Microelectromechanical Systems* 20 (1 2011), pp. 213–220. DOI: 10.1109/jmems.2010.2093568.

[51] L. Djoumi, M. Vanotti, and V. Blondeau-Pâtissier. “Real time cascade impactor based on surface acoustic wave delay lines for pm10 and pm2.5 mass concentration measurement”. In: *Sensors* 18 (1 2018), p. 255. DOI: 10.3390/s18010255.

[52] S. Nannu Shankar et al. “Assessment of scanning mobility particle sizer (smps) for online monitoring of delivered dose in an in vitro aerosol exposure system”. In: *Toxicology in Vitro* 92 (2023), p. 105650. DOI: 10.1016/j.tiv.2023.105650.

[53] J. G. Watson et al. “Comparison of four scanning mobility particle sizers at the fresno supersite”. In: *Particuology* 9 (3 2011), pp. 204–209. DOI: 10.1016/j.partic.2011.03.002.

[54] M. Marjamäki et al. “Performance evaluation of the electrical low-pressure impactor (elpi)”. In: *Journal of Aerosol Science* 31 (2 2000), pp. 249–261. DOI: 10.1016/s0021-8502(99)00052-x.

[55] Y. Wang et al. “An aerosol sensor for pm1 concentration detection based on 3d printed virtual impactor and saw sensor”. In: *Sensors and Actuators A: Physical* 288 (2019), pp. 67–74. DOI: 10.1016/j.sna.2019.01.013.

[56] Kevin Krogsøe, Morten Henneberg, and René Eriksen. “Model of a Light Extinction Sensor for Assessing Wear Particle Distribution in a Lubricated Oil System”. In: *Sensors* 18 (Nov. 2018), p. 4091. DOI: 10.3390/s18124091.

[57] Velimir Petrovic et al. “The possibilities for measurement and characterization of diesel engine fine particles: A review”. In: *Thermal Science* 15 (Jan. 2011), pp. 915–938. DOI: 10.2298/TSCI110509092P.

[58] Ann-Charlotte Larsson. “Study of Catalyst Deactivation in Three Different Industrial Processes”. In: (Jan. 2007).

[59] M. S. Hanay et al. “Inertial imaging with nanomechanical systems”. In: *Nature Nanotechnology* 10 (4 2015), pp. 339–344. DOI: 10.1038/nnano.2015.32.

[60] J. E. Sader et al. “Mass spectrometry using nanomechanical systems: beyond the point-mass approximation”. In: *Nano Letters* 18 (3 2018), pp. 1608–1614. DOI: 10.1021/acs.nanolett.7b04301.

[61] J. Yang and J. Lu. “Study of size-related sensitivity of surface acoustic wave sensor towards particulate matter sized particles using finite element and experimental methods”. In: *AIP Advances* 10 (2 2020). DOI: 10.1063/1.5140066.

[62] J. Yang and H. Chen. “A novel method of studying the micro-contact using surface acoustic wave sensor”. In: *Sensor Review* 36 (4 2016), pp. 421–428. DOI: 10.1108/sr-10-2015-0162.

[63] D. Shen et al. “New cut angle quartz crystal microbalance with low frequency–temperature coefficients in an aqueous phase”. In: *Talanta* 76 (4 2008), pp. 803–808. DOI: 10.1016/j.talanta.2008.04.028.

[64] A. Will□Cole et al. “Tutorial: piezoelectric and magnetoelectric n/mems—materials, devices, and applications”. In: *Journal of Applied Physics* 131 (24 2022). DOI: 10.1063/5.0094364.

[65] M. Akiyama et al. “Enhancement of piezoelectric response in scandium aluminum nitride alloy thin films prepared by dual reactive cosputtering”. In: *Advanced Materials* 21 (5 2008), pp. 593–596. DOI: 10.1002/adma.200802611.

[66] R. F. Schmitt et al. “Bulk acoustic wave modes in quartz for sensing measurand-induced mechanical and electrical property changes”. In: *Sensors and Actuators B: Chemical* 76 (1-3 2001), pp. 95–102. DOI: 10.1016/s0925-4005(01)00591-3.

[67] W. R. Ali and M. Prasad. “Piezoelectric mems based acoustic sensors: a review”. In: *Sensors and Actuators A: Physical* 301 (2020), p. 111756. DOI: 10.1016/j.sna.2019.111756.

[68] Darrell W Pepper and Juan C Heinrich. *The finite element method: basic concepts and applications*. Taylor & Francis, 2005.

[69] S. Maouhoub, Y. Aoura, and A. Mir. “Fem simulation of aln thin layers on diamond substrates for high frequency saw devices”. In: *Diamond and Related Materials* 62 (2016), pp. 7–13. DOI: 10.1016/j.diamond.2015.12.004.

[70] D. Liufu and K. C. Kao. “Piezoelectric, dielectric, and interfacial properties of aluminum nitride films”. In: *Journal of Vacuum Science Amp; Technology A: Vacuum, Surfaces, and Films* 16 (4 1998), pp. 2360–2366. DOI: 10.1116/1.581352.

[71] M. P. d. Cunha. “Effects of layer thickness for saw, psaw, and hvpsaw devices”. In: *IEEE Transactions on Ultrasonics, Ferroelectrics and Frequency Control* 48 (1 2001), pp. 93–99. DOI: 10.1109/58.895914.

[72] A. Ababneh et al. “The influence of sputter deposition parameters on piezoelectric and mechanical properties of aln thin films”. In: *Materials Science and Engineering: B* 172 (3 2010), pp. 253–258. DOI: 10.1016/j.mseb.2010.05.026.

[73] X. Ye et al. “Studies of a high-sensitive surface acoustic wave sensor for passive wireless blood pressure measurement”. In: *Sensors and Actuators A: Physical* 169 (1 2011), pp. 74–82. DOI: 10.1016/j.sna.2011.05.022.

[74] D. Bell and R. Li. “Surface-acoustic-wave resonators”. In: *Proceedings of the IEEE* 64 (5 1976), pp. 711–721. DOI: 10.1109/proc.1976.10200.

[75] W. Soluch. “Scattering analysis of two-port SAW resonators”. In: *IEEE Transactions on Ultrasonics, Ferroelectrics, and Frequency Control* 48.3 (2001), pp. 769–772. DOI: 10.1109/58.920709.

A

Cross structure SAW resonator fabrication list

Nr. Device	low frequency(MHz)	high frequency(MHz)	Total number of IDT&REF	IDT:REF
1	95	276	20	1:3
2				1:1
3				3:1
4			40	1:3
5				1:1
6				3:1
7	95	495	20	1:3
8				1:1
9				3:1
10			40	1:3
11				1:1
12				3:1
13	112	276	20	1:3
14				1:1
15				3:1
16			40	1:3
17				1:1
18				3:1
19	112	495	20	1:3
20				1:1
21				3:1
22			40	1:3
23				1:1
24				3:1

Figure A.1: Fabrication list

B

AlN SAW resonator fabrication flowchart

STARTING MATERIAL

Use high resistivity wafers, with the following specifications:

DSP Si Wafers 500um

Type: p-doped

Orientation: <100>

Resistivity: >1000ohm-cm

Thickness: 500 um ± 10 um

Diameter: 100.0 mm ± 0.5 mm

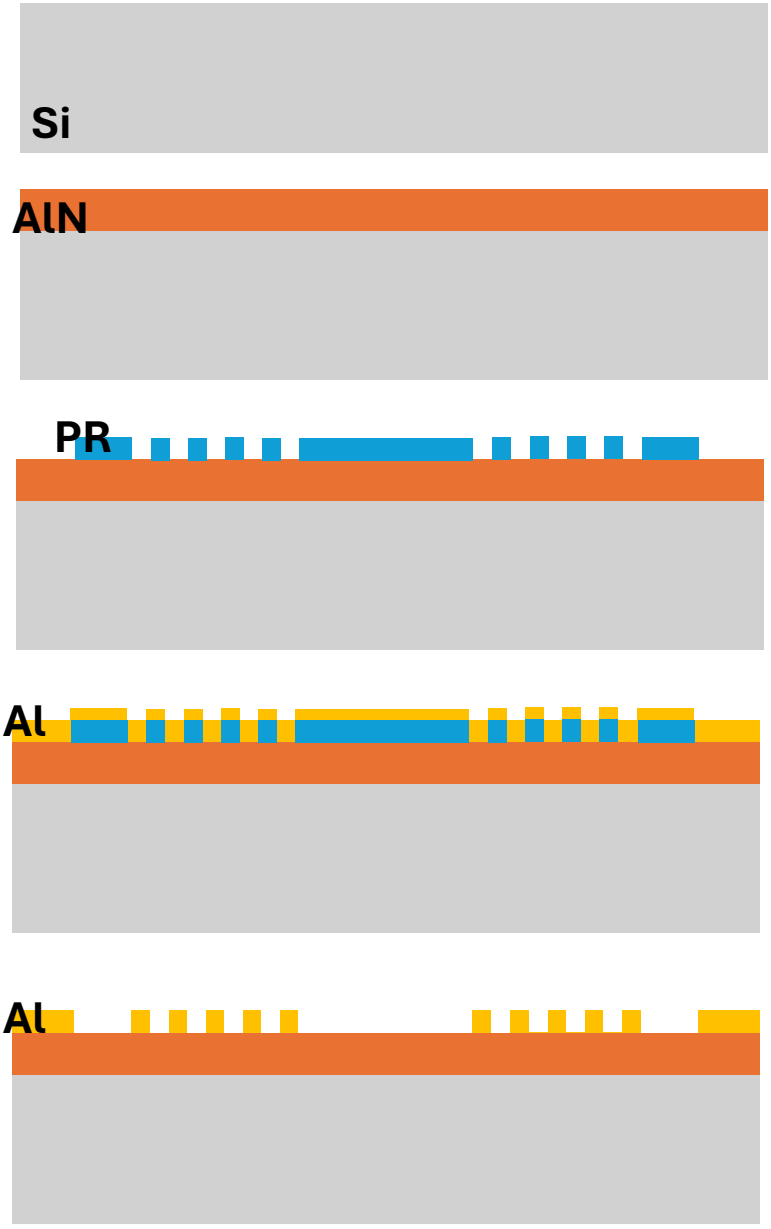

1. WAFER NUMBERING

Note down the series code on the wafer.

2. AlN deposition

Use the TRIKON SIGMA DC magnetron sputtering reactor for the deposition of a 1 um thick aluminum nitride layer on the wafers.

(Use the reactive sputtering mode, the power with the frequency of 250 kHz and pulse width of 1616 ns.)

Recipe: AlN_1um_400C_LS

3. MEASUREMENT

Ellipsometer measure the thickness of AlN. (recipes of AlN)

Or dry etching AlN to test thickness (DEKTAK)

Take part of the wafers XRD outside cleanroom (3ME?)

4. COATING

Use the coater station of the EVG120 system to coat the wafers with photoresist. The process consists of:

- a treatment with HMDS (hexamethyldisilazane) vapor, with nitrogen as a carrier gas
- spin coating of nLOF 2020 negative photo resist, dispensed by a pump.
  （bright field mask）
- a Soft Bake (SB) at 95 °C for 1.5 min

Always check the temperature of the hotplate and relative humidity (48 ± 2 %) in the room before coating, and follow the instructions for this equipment.

Test different resist thickness

Co - Nlof - 1,5µm - no EBR (start trying)

Co - Nlof - 2,0µm - no EBR (recommend)

Co - Nlof - 3,0µm - no EBR

Co –Nlof - 3,5µm - no EBR

5. ALIGNMENT AND EXPOSURE

Processing will be performed on the ASML PAS5500/80 automatic wafer stepper.

Follow the operating instructions from the manual when using this machine.

Expose mask with the correct litho job and exposure energy on AlN.

Test exposure energy value using litho-test masks with batch type M(atrix):

6. DEVELOPMENT

Use the EVG 120 Coater/developer to develop the wafers, and follow the instructions specified for this equipment.

Use development program: **Only –X-link bake**".

7. DEVELOPMENT

Use the developer station of the EVG120 system to develop the wafers. The process consists of:

- a post-exposure bake at 115 °C for 90 seconds
- developing with Shipley MF322 with a single puddle process
- a hard bake at 100 °C for 90 seconds

Always follow the instructions for this equipment.

Use development program: **Dev –Lift off**".

8. LONG HARD BAKE (additional)
   Memmert Oven

9. INSPECTION: LINEWIDTH AND OVERLAY

Visually inspect the wafers through a microscope. Check the resist edge structures and the open areas.

10. TEPLA: O2 plasma Cleaning

Plasma flash: Use the Tepla plasma system to remove the photoresist rests in an oxygen plasma.

Follow the instructions specified for the Tepla stripper, and use the quartz carrier.

Use Program # 2, Flash

Remark: Tepla should be at room temperature before starting.

11. EVAPORATION (Al 200nm)

CHA

Remark: after evaporation No steps in cleanroom 100 anymore (contamination)

Use dedicated holders, tweezers, lift-off beakers, etc.

12. LIFT OFF (CR10k wet benches, Fume Hood 5)

Lift-off procedure:

- Switch on Temperature switch to 70°C

- Put a beaker with DI – water in the Ultra Sone Bath Heat up to 70°C
- Put the beaker with NI555 into the ultrasonic bath where you can heat up the NI555 to 70°C
- Put the lift-off wafer in a single wafer holder or carrier.
- Put the holder/carrier in the NI555 beaker.
- Switch on the Ultra Sone bath

Remark: Put in DI water to rinse the wafer for 5 min every time before checking the wafer

Turn down the power and leave the wafers in the beaker overnight.

13. RINSING AND DRYING

Rinse the wafer with DI-water in a beaker for 5 minutes.

Dry the wafer with Nitrogen gun

or with the single wafer dryer (with contaminated chuck).

C

VNA probe station manual

VNA probe station manual

Qiuxuan Wang, Chong Zhan, July-2024

Location: EWI 21st floor, Earl McCune Lab

Person in charge (2024): Juan Bueno Lopez

In the first few times using the probe station and vector network analyzer, you should measure together with Juan.

Always reserve the setup before use.

Probe station setup:

1. Connect the vacuum tube (in red) with the vacuum channel (close to the electric socket of the table) and probe station;

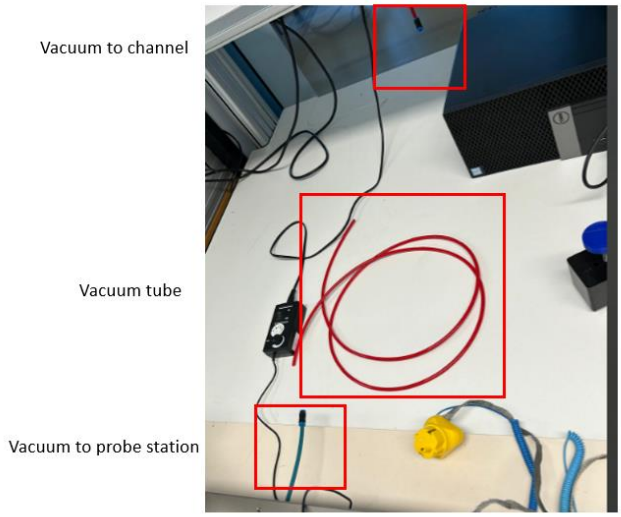

2. Switch on the vacuum controller (both switch and valve) around the room corner (North-East);

Vacuum switch Vacuum valve

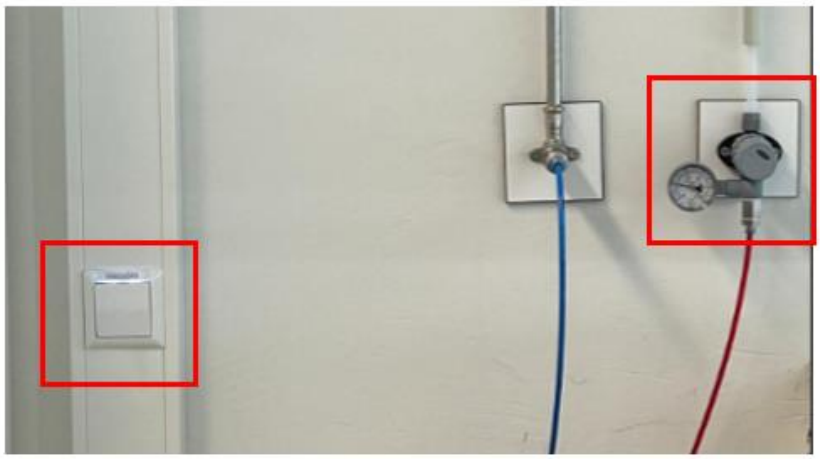

3. Turn on the microscope light;

Microscope light

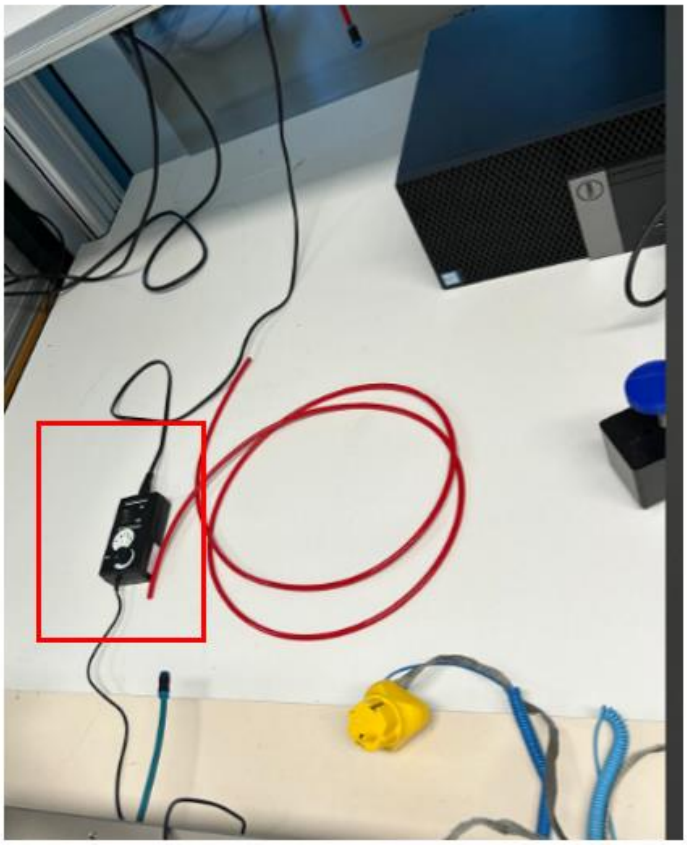

4. Use the blue knob to fix the probe arm (there are 90-degree and 180-degree probe arm options); -"fix" means that the probe arm cannot rotate or move along the slot, if it is not fixed try to ask the person in charge for help.
5. Find 2 probe needles (normally, use the blue pairs of needle otherwise the probe arm is not high enough; size info can be found on the probe needle) with correct pitch (needle distance) that can fit your design;

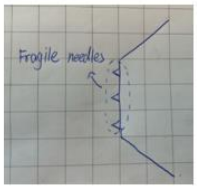

Size info: GSG 100um

Cross means broken

6. Adjust the height of the probe arm and vacuum chunk;
   !! **Make sure when the probes are lifted up**, there is enough space between the probe tip and the calibration kit or wafer on the vacuum chunk
   Also make sure the probes can be loaded on the wafer within the manipulator moving range.

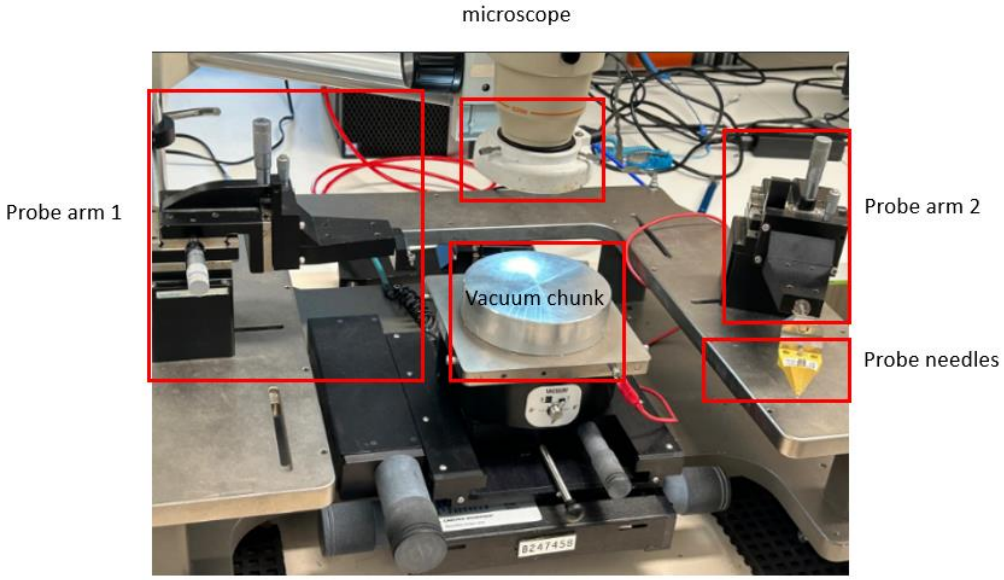

7. Take out the probe needle (before mounting to lowest probe arm, make sure the probe needle won't touch the vacuum chunk) and mount it on the probe arm (never touch the front side of probe needle!!!)(put the probe arm at an angle temporarily can make the mounting easier) with **hexagonal screws** (hexagonal screwdriver can be found in **general tools box**);
8. Take out a **VNA**, its power charge cable, and a USBA to USBC data cable from the **south shelf**; (cable usage and calibration settings will be stored in the VNA you used last time, so try to use the VNA with the **same series number** every time)

9. Connect the power charge cable to the VNA, and connect the data cable between the VNA and the PC(normally where you using the probe station, and always use blue USBA to connect with blue USBA hole on PC) in the lab;
10. Take out two SMA cables (long enough, and equal length to make it symmetric) from the SMA cable box, and take out two 90-degree SMA connectors from the SMA connectors/adapters box;

11. Remove the blue cup on the two probe needles, and connect the revealed SMA connector with the 90-degree SMA connectors found in the last step, then connect two 90-degree SMA connectors with the VNA port1 and port2 using the SMA cable found in the last step; (after mounting those by hands, using torque wrenches to check whether they are mounted tightly!!!)

Probe loading:

Probes should always be up (turn anti-clockwise to the end) except the moment you need signals through your device.

Make sure the device under measurement is fixed either with the vacuum or tape.

GSG probes are usually used with three tips in a line on the probe front.

1. Focus the microscope on your device pad.
   Try to find the probe you want to load under the microscope. It should be blurry as it is lifted up and out of focus.
2. Slowly and carefully turn down the probe until it is about to become clear. It should almost touch the device at this point. (Sometimes there are reflections of the probe from your metal pad to help you tell how close the probe is to the device.)
3. Further turn down the probe even slower, you should see the three points of probe slide slightly as you turn down the probe in horizontal direction. This is because the probe front has touched the device, further pressing down will make it slide.
4. The probe is loaded. Generally, do not turn down the probe anymore. You can observe some signals from S11 or S22. When both two probes are loaded, you can also observe signals from S12 and S21.
5. After each single measurement, lift the probes up. Protect it from damage.

Software settings:

1. Login to the PC in the lab with your tud id;
2. Switch on the button on the VNA;
3. Open the VNA software on PC;
4. Set the start and stop frequency (range), frequency interval, IF bandwidth (usually 1kHz, lower IF bandwidth means a more stable signal but longer freq sweeping time) and Power (due to device limitation can't be more than 0dBm);- every time you want to measure with a larger freq range the calibration below should be rebuilt;

Calibration settings: (Ask Juan about the calibration kit for your measurements)

1. Find the calibration kit in the calibration kit box, the normally used model is P/N:101-190, open the datasheet (which tells you the open, short, load and through configures) of the corresponding calibration kit (datasheet of P/N:101-190 has been attached at the end of this doc, if you need to use other calibration kits just search: "Impedance Standard Substate P/N" with its <*model number*>);

2. Take out calibration kit from its container, use thin white fabric tape to tape it on vacuum chunk;

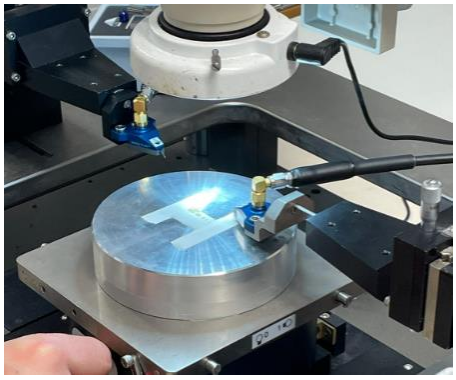

3. Open the “smart calibration” menu from the software, and make selections as following figures;

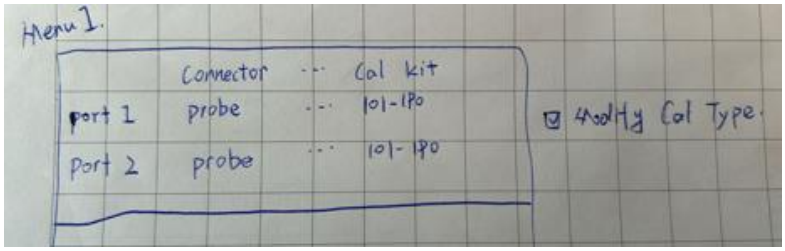

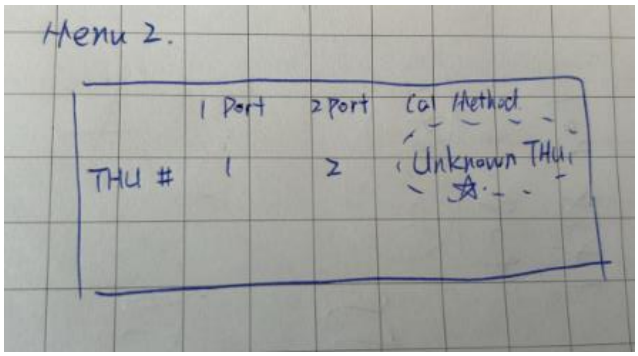

4. Then follow the instructions on the software and land probe needles on the calibration kit at open, short, load, and through positions (use the datasheet as the reference can make it easy);
   IMP: probe needles are very fragile and valuable devices. If you are not experienced with them. Please ask the person in charge to train you!
5. After seven calibration measurements (port1 open, port1 short, port1 load, port2 open, port2 short, port2 load, port1-port2 through), you can save your calibration settings on this VNA (remember the series number, use the same one next time)

Expected seven calibration measurement results and simple explanation:

The single S-parameter(S11,S22) can be induced by the reflection coefficient: $\Gamma = \frac{z-z_0}{z+z_0}$, where z is the instinct device (VNA and all wires) impedance and z0 is the calibration impedance;

1. For single port Open measurement ($z_0 = \infty$): $\Gamma = \frac{z-z_0}{z+z_0} = \frac{\frac{z}{z_0}-1}{\frac{z}{z_0}+1} = -1$, which means that power transmitted from the single port is reflected totally. So, in the software S11 or S22 Open calibration is always shown 0dB;
2. For single port short measurement ($z_0 = 0$): $\Gamma = \frac{z-z_0}{z+z_0} = \frac{z}{z} = 1$, which also means that power transmitted from the single port is reflected totally. So, in the software S11 or S22 Short calibration is also always shown as 0dB;
3. But for single port Load measurement ($z_0 \approx 50\Omega$)(device impedance is also around 50Ω): $\Gamma = \frac{z-z_0}{z+z_0} = \frac{0}{z+z_0} = 0$, which means that power transmitted from the single port is consumed totally. Ideally, the S11 and S22 in the software are shown 0dB. However, due to impedance bias, the actual S11 and S22 are around -10 to -20dB;
4. For the two ports through calibration, the S12 and S21 results will change from around -70dB (no power transmitted from port1 tto port2) to around 0 dB (all power transmitted from port1 to port2)

D

15 μm diameter monodisperse silica particles

Monodisperse silica particles can be used in a variety of applications like medical diagnostics, for pharmaceutical and biotechnological purposes, in analytics, molecular biology, and others. Utilizing modified sol-gel strategies, microParticles GmbH has been developed high-quality silica particles in the nanometer and micrometer size range. The particles combine many favorable properties, such as high monodispersity (CV < 5 %), spherical shape, high optical transparency, high mechanical and thermal stability, or hydrophilic surface properties. They are non-porous and have a high density ($1.85 g/cm^3$). Our monodisperse silica particles are available in more than 70 discrete sizes with particle diameters from 100 nm to 100 μm. Diameters and size distributions are measured by differnt measuring techniques like scanning electron microscopy, Differential Sedimentation (CPS disc centrifuge), Coulter-devices, and optical microscopy. Silica particles from 100 nm - 29 μm are supplied as 5 % (w/v) aqueous suspensions, silica particles from 30 μm- 100 μm are supplied as 2.5 % (w/v) aqueous suspension.

Details of used 15 μm S2O2_R_15.0 is shown in tableb below:

Infos

Batch:	SiO_2-R-SC264-3
Mean Diameter (µm):	15.03
Standard Deviation (µm):	0.57
CV (%):	3.8
Solids Content (wt.-%):	5

E

SiO2 suspension dilution

SiO2 concentration reduction (clean with IPA)

Original concentration: $5\ wt\%\left(\frac{w}{v}\right) = 5\% \times 10mL = 0.5g$

Density of SiO2: $\rho_{sio2} = 2.65 \times 10^{-12} g/\mu m^3$

15um SiO2 sphere particle mass: $m = \rho_{sio2} \times \frac{4}{3}\pi 15^3 = 3.746 \times 10^{-8} g$

0.5g solution particle number: $\frac{0.5}{m} = 1.334757074 \times 10^7$

particle number concentration: $1.334757074 \times 10^6/mL$

50mL concentration reduction 2 times: $1.334757074 \times 10^6 \div 50 \div 50 = 533.9028296/mL$

2uL particle number: $\frac{533.9028296}{mL} \times 0.002mL = 1.067805659 = 50$

Figure E.1: SiO2 Suspension Dilution Procedures